Climatological Statistics of Extreme Geomagnetic Fluctuations with Periods from 1 s to 60 min

N. C. Rogers, J. A. Wild, E. F. Eastoe, and J. Hübert

Abstract

Extreme fluctuations in the horizontal geomagnetic field (dB_h/dt) may be generated at the Earth's surface by electrical currents in the ionosphere and magnetosphere. Using a global database of 125 magnetometers covering several decades we present occurrence statistics for fluctuations exceeding the 99.97th percentile ($P_{99.97}$) for both ramp changes (R_n) and the root-mean-square (S_n) of fluctuations over periods, τ, from 1 to 60 min and describe their variation with geomagnetic latitude and magnetic local time (MLT). Rates of exceedance are explained by reference to the magneto-ionospheric processes dominant in different latitude and MLT sectors, including ULF waves, interplanetary shocks, auroral substorm currents, and travelling convection vortices. By fitting Generalised Pareto tail distributions above $P_{99.97}$ we predict return levels (RLs) for R_n and S_n over return periods up to 500 years. $P_{99.97}$ and RLs increase monotonically with frequency ($1/\tau$) (with a few exceptions at auroral latitudes) and this is well modelled by quadratic functions whose coefficients vary smoothly with latitude. For UK magnetometers providing 1-s cadence measurements, the analysis is extended to cover periods from 1 to 60 seconds and empirical Magnetotelluric Transfer functions are used to predict percentiles and return levels of the geoelectric field over a wide frequency range (2×10^{-4} to 4×10^{-2} Hz) assuming a sinusoidal field fluctuation. These results help identify the principal causes of field fluctuations leading to extreme geomagnetically induced currents (GIC) in ground infrastructure over a range of timescales and they inform the choice of frequency dependence to use with dB_h/dt as a GIC proxy.

Key points

1. Statistics of extreme geomagnetic fluctuation (dB_h/dt) are determined from global magnetometer records over several decades.
2. The frequency (or timescale) dependence of dB_h/dt is well modelled by quadratic functions parameterised by geomagnetic latitude.
3. Electric fields calculated at 3 UK sites peak at periods of 20 min at the 99.97th percentile but 0.5–2 min for 1/100-year events.

Plain language summary

On rare occasions, an eruption on the sun's surface sends a cloud of energetic electrically-charged particles out into interplanetary space. When this arrives at the Earth it can cause large electrical currents to flow around the magnetic field surrounding the Earth (the 'magnetosphere') and through the upper atmosphere. These currents are detected on the ground as fluctuations in the magnetic field and may induce unwanted electrical currents in high-voltage power lines or other long metallic cables and pipelines. The rate of change of the magnetic field is used together with measurements of ground conductivity to calculate the electric field that drives such 'geomagnetically induced currents'. In this study we report the rate of occurrence of extremely rapid fluctuations in the magnetic field, and how this depends on latitude and time of day. We model the dependence of the size of the fluctuations on their timescales since this is important for estimating the subsequent response of the power grid. The patterns of extreme occurrences are explained by reference to known electrical current systems and waves in the magnetosphere and upper atmosphere, and we use statistical methods to predict the size of fluctuations expected as rarely as once in 500 years.

1 Introduction

Large electrical currents are occasionally induced in ground-based infrastructure as a result of rare and intense currents in the ionosphere or magnetosphere. These Geomagnetically Induced Currents (GIC) have been identified as a substantial hazard to national infrastructure (Cannon et al., 2013; Hapgood et al., 2021) since they may cause catastrophic failure in high-voltage electricity supply networks (Gaunt, 2016; Oyedokun & Cilliers, 2018; Thomson et al., 2010), damage long-cable communication systems (Nevanlinna et al., 2001) and cause railway signalling errors (Boteler, 2021; Eroshenko et al., 2010; Wik et al., 2009). The cumulative effect of GICs above a certain threshold may also cause corrosion in oil and gas pipelines (Boteler, 2000; Pulkkinen et al., 2001). The science of GICs and their effects is reviewed in (Knipp, 2011, Chapter 13) and (Buzulukova, 2017, Chapter 8).

Modelling the risk of extreme GICs requires a statistical characterisation of the geoelectric field, $\boldsymbol{E}$, induced by electrical currents in the ionosphere and magnetosphere. This information may, for example, be combined with a model of electrical impedances in a high-voltage (HV) electricity network (Boteler & Pirjola, 2017) to determine the ‘return level’ (RL) of GIC expected in a ‘return period’ of 100 years or more. Direct measurements of $\boldsymbol{E}$ are often subject to contamination from anthropogenic electromagnetic interference and require an experienced expert to remove noise and biases (Kelbert et al., 2017). They are also not global in extent, and do not cover the decades required for accurate prediction over long return periods. For climatological studies it is therefore expedient to instead use an archive of measurements of the rate of change of the horizontal component of the geomagnetic field, dB_h/dt, measured at ground level. Using Faraday’s law of induction (Faraday, 1832) and magneto-telluric (MT) theory (Cagniard, 1953; Chave & Jones, 2012) these may be combined with a model of the local ground conductivity to determine climatological statistics for $\boldsymbol{E}$. Alternatively, $\boldsymbol{E}$ may be derived using collocated measurements of ground impedance at a magnetometer site.

The calculation of $\boldsymbol{E}$ requires knowledge of both the temporal spectrum of geomagnetic oscillations and the frequency dependence of the surface impedance. Databases of impedance tensors are increasingly available for public use (e.g. Kelbert et al. 2011; Kelbert et al. 2018) and can cover a wide frequency range corresponding to periods from milliseconds to hours. The most effective source of geoelectric fields producing damaging GIC in power transmission lines lie in 1–1000 s period oscillations (Kappenman, 2004; Barnes et al., 1991) and electricity companies have identified that fluctuations on timescales from tens of seconds to over an hour have led to vulnerability of high-voltage (HV) electricity networks to GIC (e.g., NERC, 2017; Girgis & Vedante, 2012). A well-reported example is the geomagnetic storm of 13 March 1989 in which the 21 GW Hydro-Québec power supply failed for nine hours following horizontal geomagnetic field fluctuations $|dB_h/dt|$ of approximately 500 nT/minute (p.640, Knipp, 2011).

The frequency of the induced E field fluctuations and consequent GICs is much less than the frequency of high-voltage electricity networks (50 or 60 Hz) and so is often modelled as a quasi-direct current. Currents of more than a few amperes sustained over periods similar to the thermal time constants of the components of a high-voltage transformer – typically 30–45 minutes – may cause irreversible damage resulting in power failures (p.8, IEEE, 2015; Girgis & Vedante, 2012; Erinmez et al., 2002; Molinski, 2002; NERC, 2017). GICs generated by field fluctuations with periods longer than 1 hour have amplitudes too small to be of concern, whilst sub- 1-s fluctuations are heavily damped by inductances in electric power systems (Boteler & Pirjola, 2017). Understanding the climatology of extreme $|dB_h/dt|$ over periods from 1 s to 1 hour should, therefore, help to quantify the GIC risk to electrical power systems.

Large-scale statistical surveys often exploit measurements at 1-min resolution, in large part enabled by the successful SuperMAG project (Gjerloev, 2011), thus many have examined only the 1-minute changes in B_h, (denoted R_1), with this metric being adopted as a proxy for GICs (e.g. Viljanen et al., 2001, 2015; Thomson et al., 2011). However, probability distributions of $|dB_h/dt|$ are observed to depend strongly on the time resolution (or sample averaging period) of the *B* field measurements, with lower amplitudes at longer sampling intervals due to the effect of smoothing. In recent years, an increasing number of magnetometer operators have offered users measurements at 1-s cadence and so the question arises as to which temporal resolution to apply when using $|dB_h/dt|$ as a proxy indicator for GIC. Modelling by (Pulkkinen et al., 2006) showed that smoothing the *B*-field components from their native resolution of 1 s up to 60 s reduced the amplitude of $|dB_h/dt|$ by 80% whilst the computed peak E-field amplitudes were reduced by only 20%, the inference being that a 60-s (but no more) sample interval is acceptable as a proxy to use for *E*-field (and hence GIC) calculations. Other studies have noted that rather than taking R_1 as a proxy for GIC, a better performing indicator was obtained by taking an average dB_h/dt over 20-minutes (Tõth et al., 2014) or 30 minutes (Viljanen et al., 2015), whilst others have used the hourly range or standard deviation (Beamish et al. 2002; Nikitina et al., 2016; Danskin & Lotz, 2015) or 3-hourly range indices as a proxy (Trichtchenko & Boteler, 2004).

In several cases, the magnitude of B_h relative to its quiet-day value (often denoted ΔH) has provided a better proxy for GIC than dB_h/dt (Pulkkinen et al., 2010; Tõth et al., 2014; Watari et al., 2009). Pirjola (2010) showed how this is more likely to arise in regions for which there is an upper, highly conductive layer overlying a deeper layer of low conductivity. Heyns et al. (2020) presented examples of GIC amplitudes and phases matching closely to the 20-min period fluctuations of the field (ΔH) which were poorly represented by high-cadence dB_h/dt indicators, whilst dB_h/dt was a better indicator of the rapid field variation that occurred during Sudden Commencements, which often initiate geomagnetic storms. Heyns et al. (2020) explained that this is because the *B* field (or ΔH) has low-frequency components that are deweighted when taking the time derivative – for example, if $B_h = B_0 \exp(i\omega t)$ then frequency components of $|dB_h/dt|$ are weighted by the factor $1/\omega$. Consequently, 1-s resolution dB_h/dt measurements ($R_{1/60}$) would be even less effective as a proxy for GIC (compared to R_1) for GIC caused by field fluctuations of a much longer period. Power networks can respond strongly to *B*-field fluctuations over tens of minutes, indicative of finite reactive impedances in the network components, and assumptions that the geomagnetic driving is d.c. in nature may be insufficient to replicate the observed GIC (Heyns et al., 2020; Jankee et al., 2020).

The study of extreme geomagnetic fluctuations over a range of periods yields much information about the causes and impacts of GIC as well as the drivers of these fluctuations. The ionospheric and magnetospheric processes contributing to dB_h/dt over a 1-min period will differ greatly from those at 60 min and will depend on the latitude, magnetic local time (MLT), season, and other factors. The principal drivers of short transients (timescales of minutes) may be categorised into the following phenomena:

1. **Sudden Commencements (SC)**: Interplanetary shocks arriving in the solar wind, which generate a sudden eastward (dusk-to-dawn) Chapman-Ferraro current at the dayside magnetopause, are observed as Sudden Commencements (SC) in magnetograms (Fiori et al., 2014; Kappenman, 2003; Smith et al., 2019). The characteristic rapid magnetic field variation may be short-lived, lasting several minutes or up to an hour (Knipp, 2011, p.496), and are associated with dB_h/dt of up to 30 nT/min at low geomagnetic latitudes (< 40°) or up to a maximum of 270 nT/min in the auroral zone (approximately 65° geomagnetic latitude) (Fiori et al., 2014).
2. **Auroral substorm onsets**: A substorm is the sudden brightening and expansion of auroral arcs resulting from bursts of energetic electron precipitation from the magnetotail (Akasofu, 2017; Ieda et al., 2018). This enhances the ionisation and electrical conductivity of the ionospheric *E* region allowing strong Hall currents to flow, most often in a westward direction which manifest in magnetograms as a rapid decline in the north component of the geomagnetic field, B_N. Substorm onsets have been categorised by Newell & Gjerloev (2011) from the SML geomagnetic index (which measures the lower envelope of B_N) as a reduction of at least 45 nT over 3 minutes followed by a mean level at least 100 nT below the initial value during the half-hour following onset.
3. **Day-time Magnetic Impulse Events (MIE)**: Pairs of up- and down- field aligned currents generated by a pulse in dynamic pressure at the dayside magnetopause couple into the ionosphere as Travelling Convection Vortices (TCV) at latitudes in the vicinity of the dayside cusp/cleft (approximately 77-78° magnetic) (Zesta et al., 2002; Kataoka, 2003; Engebretson et al., 2013; Friis-Christensen et al., 1988; Lanzerotti et al., 1991). Magnetometers in this region observe the ionospheric Hall current loops (a pair of vortices) as isolated magnetic impulse events (MIE) in magnetograms, lasting typically 5-15 minutes with amplitudes of typically 50–200 nT or up to a maximum of 400 nT (Kataoka et al., 2003; Lanzerotti et al., 1991). Several mechanisms have been postulated to explain the generation of TCVs near the dayside magnetopause, including bursts of magnetic field line reconnection (flux transfer events), solar wind pressure pulses, plasma injections into the low-latitude boundary layer, Kelvin-Helmholtz instabilities, and perturbations of the ion foreshock upstream of the Earth's bow shock (see references in Kataoka et al., 2003 and Engebretson et al., 2013). In general, TCVs are defined so as to exclude sudden commencement perturbations associated with a large interplanetary shock (e.g. Pilipenko et al., 2019).
4. **Night-time Magnetic Perturbation Events (MPE)**: MPEs are a broad class of large (hundreds of nT), localised, 5-10 min unipolar or bipolar pulses of B_h which occur in the auroral zone during substorms, but are not necessarily associated with substorm onsets (Engebretson et al., 2019a,b, 2020, 2021; Belakhovsky et al., 2019; Dimmock et al., 2019; Apatenkov et al., 2020; Viljanen, 1997). They arise from transient phenomena in the magnetotail such as bursty bulk flows (BBFs) (Angelopoulos et al., 1992; Wei et al., 2021), dipolarising flux bundles (Liu et al., 2014), poleward-expanding discrete aurorae passing over the magnetometer site (Ngwira et al., 2018), and small-scale rapidly moving ionospheric current vortices (Apatenkov et al., 2020).

A significant number of GIC events occur under geomagnetic storm conditions at auroral and mid-latitudes due to sustained ULF pulsations in the Pc5 band (2.5–10 min period field oscillations (Baker et al., 2003; McPherron, 2005; Pilipenko et al., 2010; Ziesolleck & McDiarmid, 1995)). These may be driven by Alfvén wave Kelvin-Helmholtz instabilities in the magnetosphere and are often initiated by the arrival of a shock in the solar wind or a high-speed solar wind stream (>500 km/s) (Engebretson et al., 1998; Pahud et al., 2009; Vennerstrøm, 1999; Zhang et al., 2010; Hao et al., 2019). In addition, auroral omega bands (Apatenkov et al., 2020; Belakhovsky et al., 2019) may manifest in magnetograms as quasi-periodic (4-40 min) "Pi3" or "Ps6" geomagnetic fluctuations on the morning side during the recovery phases of substorms (Jorgensen et al., 1999; Saito, 1978; Wild et al., 2000) or during substorm expansions in the midnight sector (Wild et al., 2011).

B-field fluctuations over tens of minutes may also arise from the expansion and recovery phases of substorms in the auroral zone (Freeman et al., 2019; Pothier et al., 2015): The substorm expansion phase typically lasts 25–40 minutes (Pothier et al., 2015) followed by a more gradual recovery phase. Changes over an hour or more may arise from slow changes and movements of an electrojet over a magnetometer station or from gradual changes of the magnetospheric inner ring current intensity during the main and recovery phases of a geomagnetic storm.

At very high latitudes (poleward of the dayside cusp) and under conditions of northward interplanetary magnetic field (IMF) and large dipole tilt (e.g. at summer noon), magnetic fluctuations may be associated with the merging of 'overdraped' tail-lobe field lines with the IMF (Crooker, 1992; Watanabe et al. 2005). Rogers et al. (2020) postulated that field-line reconnections may drive impulsive 'Region-0' field-aligned currents (Wang et al. 2008; Milan et al. 2017) into this region that could manifest as large $|dB_h/dt|$ fluctuations at the surface.

In this paper we have extended a global climatological statistical model of extreme 1-minute fluctuations, R_1, (Rogers et al., 2020) to include the magnitude and frequency of occurrence of extreme $|dB_h/dt|$ over sampling periods between 1 and 60 minutes, both as ramp changes (applying a moving average of the geomagnetic field measurements) and as a root-mean-square (RMS) of the R_1 values over n-minute periods that we denote S_n for n = 1–60 (defined explicitly in Section 2). The latter is a measure of the sustained power in extreme geomagnetic field fluctuations, which is important in modelling the risk to transformer components due to heating, for example. Our study complements that of Love et al. (2016a) who provided an analysis of extreme $|dB_h/dt|$ over 1- and 10-minute periods, (R_1 and R_{10}), and the RMS of R_1 over 10 minutes (S_{10}). Wintoft (2005) and Wintoft et al. (2005) also chose to study S_{10} as a predictor of the RMS GIC amplitude. Part of our study will focus on three UK magnetometer sites, and as such complements the work of Beamish et al. (2002) – who examined the hourly standard deviation of 1-min *B*-field north and east components (independently), a measure similar to the S_{60} calculated in this paper – and the works of Beggan et al. (2013) and Beggan (2015), who estimated extreme *E*-field and GICs for the UK national grid at 100- and 200-year return periods using UK ground conductivity models for 2 and 10-min period fluctuations of the inducing *B*-field, with amplitudes inferred from predicted extremes of R_1 presented by Thomson et al., (2011).

In section 2 we describe the processing of magnetometer measurements data set and the determination of extreme values for $|dB_h/dt|$ as both ramp changes and RMS fluctuations. Section 3 presents the latitude and MLT distributions of large percentiles and projected extreme values for a range of sampling frequencies and develops a global model to characterise the dependences on sampling frequency. The frequency range is extended up to 1 Hz sampling for three UK sites, and for these locations empirical MT transfer functions (surface impedance matrices) are used to predict high percentiles and extreme values of the geoelectric field.

2 Measurements

Magnetic field measurements (magnetograms) were obtained from 125 magnetometers in the global SuperMAG collaboration (Gjerloev, 2011) at sites for which at least 20 years of data was available, with an average of 28 years' data per site. Table 1 provides the locations of these magnetometer sites in geodetic and corrected geomagnetic (CG) coordinates (Laundal & Richmond, 2017; Shepherd, 2014). Due to the secular variation of the Earth's main field, CG coordinates are given as averages over all years in which magnetometer data was available at each site. In this paper we consider only the north and east components of the magnetic field (B_N and B_E, respectively) in local magnetic coordinates (Gjerloev, 2012) neglecting the downward vertical field component, B_z, which contributes little to GICs in surface-based infrastructure. The magnetograms provided by SuperMAG had already been cleaned and manually inspected to remove most artificial sudden changes in the baseline (offsets), spikes, and gradual slopes (Gjerloev, 2012). Nonetheless, as a further check, all data in weeks containing R_1 peaks above the 99.97th percentile ($P_{99.97}$) were visually inspected and obvious artefacts (such as large spikes, step changes, and instrument saturation effects) were replaced by data gaps, as described in (Rogers et al., 2020).

At each magnetometer, the 'ramp' change in the horizontal component of $\boldsymbol{B}$ over n-minute intervals was defined as

$$\boldsymbol{R_n} = \{R_n(i):\ i\ = 1,2,3, \ldots, k\} \tag{1}$$

$$R_n(i) = \sqrt{\left(\frac{B_N(i) - B_N(i\text{-}n)}{n\Delta t}\right)^2 + \left(\frac{B_E(i) - B_E(i\text{-}n)}{n\Delta t}\right)^2} \tag{2}$$

where k is the number of field measurements, and Δt = 1 minute was the cadence of the measurements. For computational efficiency, the values $\boldsymbol{R_n}$ were calculated using n-point moving-average filters on the 1-minute first differences of B_N and B_E. Intervals containing missing data were excluded from the analysis. The statistics of $\boldsymbol{R_1}$ (1-min field fluctuations) were modelled in (Rogers et al., 2020). The definition in (2) ensures that statistics of the induced E-field magnitude, $|E| = \sqrt{E_N^2 + E_E^2}$ will be directly proportional to R_n and is the formula adopted by Freeman et al. (2019), Smith et al. (2019), Wintoft et al. (2015, 2016), Ngwira et al. (2018), Falayi et al. (2017), Kozyreva et al. (2018) and others. This definition of R_1 differs slightly from the first differences of B_h (i.e. $d|B_h|/dt$) computed by some authors (e.g. Love et al., 2016a; Thompson et al., 2011) particularly when there is a rapid change in field direction.

The root-mean-square of $\boldsymbol{R_1}$ over n-minute periods was defined as

$$\boldsymbol{S_n} = \{S_n(i), \qquad i\ = 1,2,3, \ldots, k\} \tag{3}$$

with

$$S_n(i)\ = \sqrt{\frac{1}{n}\sum_{j=i-n+1}^{i} R_1(j)^2} \tag{4}$$

and this was implemented in software using a convolution filter. Since we are only interested in extreme values, a high threshold for $\boldsymbol{R_n}$ and $\boldsymbol{S_n}$ was set at the 99.97th percentile level, $P_{99.97}$. The application of extreme value statistics (Coles, 2001) requires an assumption that exceedances of this threshold are temporally independent rather than clustered together. Therefore, the threshold exceedances were declustered to ensure a minimum 12 hours between clusters and only the peak value in each cluster was recorded. The magnetic local times (MLT) (Laundal & Richmond, 2017) associated with each peak were also calculated as described by Rogers et al. (2020). Declustered exceedances ($\boldsymbol{R_n} > P_{99.97}$) were then fitted to a Generalised Pareto (GP) 'tail' distribution and the fitted GP profile was used to predict return levels (RL) expected over return periods (RP) of up to 500 years (see (Rogers et al., 2020) and (Coles, 2001) for mathematical details). The analysis of extreme field fluctuations at 28 European magnetometer sites by Thomson et al. (2011) showed that the choice of a $P_{99.97}$ threshold and 12-hour declustering provides relatively stable GP coefficients whilst ensuring temporal independence of the extreme events. For consistency of approach we have therefore adopted these thresholds for our analysis of magnetometer data worldwide.

A further set of magnetometer measurements at 1-s cadence were obtained for three sites in the UK operated by the British Geological Survey, namely, HAD (Hartland, southern England, CG latitude λ = 47.55°), ESK (Eskdalemuir, southern Scotland, λ = 52.65°), and LER (Lerwick, Shetland Is, northern Scotland, λ =57.97°) (see Table 1). Data at 1-s resolution were available from 1 Jan 2001 to 14 Sep 2016 for all three sites, whilst the 1-min SuperMAG data set extended from 1 Jan 1983 to 31 December 2016 for all three sites. The data were visually inspected for weeks containing 1-s $|dB_h/dt|$ ($R_{1/60}$) exceeding the 99.97th percentile, and obvious artefacts removed in the same manner as for the 1-minute SuperMAG data set described above.

The measurement of the ground magnetic field has a long established tradition in many countries and data quality and standards are set to a high level, e.g. through INTERMAGNET (Thomson & Flower, 2021; Love & Chulliat, 2013). In contrast, long-term observations of the ground electric field are relatively rare (Beggan et al., 2021 and references therein) and more influenced by man-made electromagnetic noise due to a low signal-noise ratio. Available data sets are scarce and often discontinuous. In the UK, the ground electric field has been monitored at the three geomagnetic observatories (HAD, ESK, and LER) since 2015 with non-polarizable electrodes along north-south (N-S) and east-west (E-W) oriented baselines. (Some recent examples of these measurements are available online: http://www.geomag.bgs.ac.uk/data_service/space_weather/geoelectric.html.)

To obtain estimates of the geoelectric field for times when no data was recorded, the horizontal geoelectric field spectrum, $\boldsymbol{E}(f) = \begin{pmatrix} E_x \\ E_y \end{pmatrix}$ may be estimated from the horizontal magnetic field spectrum $\boldsymbol{B}(f) = \begin{pmatrix} B_x \\ B_y \end{pmatrix}$ via

$$\boldsymbol{E}(f) = \boldsymbol{Z}(f)\boldsymbol{B}(f) \qquad (5)$$

where $\boldsymbol{Z}(f) = \begin{pmatrix} Z_{xx} & Z_{xy} \\ Z_{yx} & Z_{yy} \end{pmatrix}$ is the complex magnetotelluric transfer function (or MT impedance tensor), and *x* and *y* refer to north and east components, respectively (e.g., Love et al., 2018, Campanyà et al., 2019, Hübert et al., 2020). Fourier transforms may be used to convert between the frequency (*f*) and time domains. $\boldsymbol{Z}$ is quasi-static and frequency-dependent and contains information about the electrical conductivity structure of the subsurface that is used for deep geophysical exploration.

Z was estimated from simultaneous measurements of the horizontal components of the ground electric and magnetic field using robust statistical approaches to minimize the influence of noise. For the estimation of ***Z*** at HAD, ESK and LER, we used six months of electric and magnetic field measurements from 2015 and applied the impedance estimation algorithm of Smirnov (2003). Further details of the procedure are given in (Beggan et al., 2021). Due to the sampling cadence of 1 s and the frequency response of the fluxgate magnetometers at the observatory sites, the impedance estimates cover a period range of 20 to 20,000 s (or $5{\times}10^{-2}$ – $5{\times}10^{-5}$ Hz).

3 Latitude, MLT, and Seasonal distribution of large R_n and S_n on timescales from 1 to 60 min

Figure 1 presents the 99.97th percentiles of a) Ramp changes (R_n) and b) RMS fluctuations (S_n) at four sampling intervals, $\tau \equiv n\,\Delta t = 1$, 10, 30, and 60 min, plotted against the mean absolute CG latitude, $|\lambda|$. Each point in the graphs represents $P_{99.97}$ at an individual magnetometer site, and the solid curves are smoothed spline fits to the data.

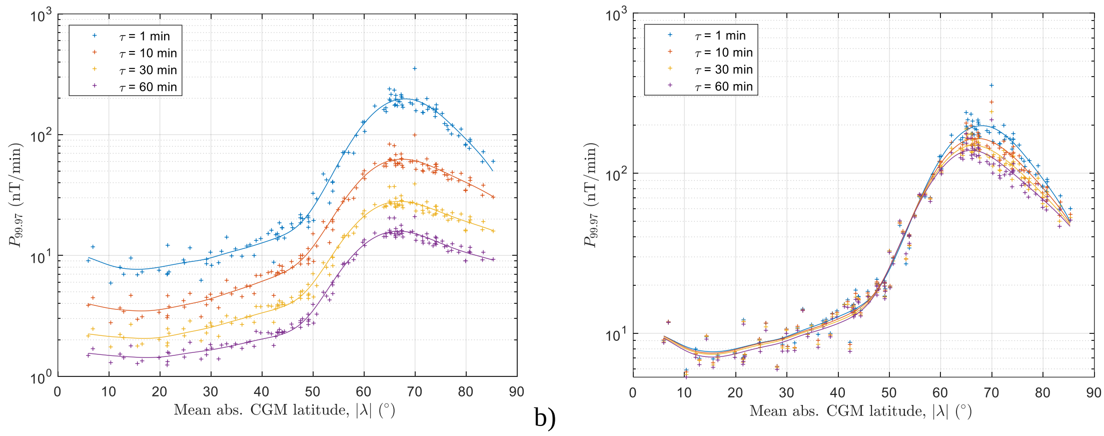

a) b)

Figure 1. 99.97th percentiles of a) ramp changes (R_1, R_{10}, R_{30}, and R_{60}) and b) RMS variations (S_1, S_{10}, S_{30}, and S_{60}). Solid lines are smoothed spline fits.

The shapes of the profiles $P_{99.97}(|\lambda|)$ are broadly similar for both R_n and S_n and for all τ, consisting of a broad maximum centred about $|\lambda| \cong 67°$, indicative of intense auroral current systems in this region, tapering to a minimum at $|\lambda| \cong 15°$ with a slight increase towards the equator. The latter is indicative of stronger disturbances near the equatorial electrojets, a narrow band of enhanced ionospheric *E*-layer currents in the region $|\lambda| < 5°$, which have previously been associated with elevated $|dB_h/dt|$ and GIC magnitudes (Adebesin et al., 2016; Pulkkinen et al., 2012; Carter et al., 2015; Ngwira et al., 2013). For ramp changes (Figure 1a) there is a strong dependence on τ and the shape of $P_{99.97}(|\lambda|)$ changes with τ (most clearly evident when comparing the curves for τ = 1 and 10 min). The dependence of the RMS magnitude on τ (Figure 1b) is, to a first approximation, flat except at latitudes above $|\lambda| \cong 60°$ where $P_{99.97}$ decreases with increasing τ. In Section 4 we shall further develop models of $P_{99.97}(|\lambda|, \tau)$ for both R_n and S_n, and present similar models for their 100-year return levels.

To gain a better understanding of the physical drivers of these large fluctuations, we first examine their magnetic local time (MLT) dependence. Figure 2 presents the probability of (declustered) peaks of $|dB_h/dt|$ exceeding

$P_{99.97}$ as a function of $|\lambda|$ and MLT. This was calculated by counting the number of peaks in 1-hour bins of MLT and 3.3° bins of $|\lambda|$, where data from multiple magnetometers were aggregated where they lay within the same latitude bin. (Bin sizes were chosen as a compromise between resolution and quantisation noise.) The bin counts were then normalised by the total number of field measurements in each bin. Panels (a–d) present the distributions for ramp changes over 1, 10, 30 and 60 min, respectively, whilst panels (e–h) present the distributions for the RMS magnitudes over 1, 10, 30 and 60 min, respectively. We have used absolute latitude on the vertical axes since the distributions of occurrence probability against (signed λ, MLT) were, to a close approximation, symmetric about λ = 0. Note that panels a) and e) are identical, which may be noted from Equation (4) with n=1. When interpreting the distributions in Figure 2 it is important to remember that the threshold $P_{99.97}$ itself varies with $|\lambda|$ (see Figure 1) and as such it is simplest to focus on the MLT distribution in each individual latitude band. It is also important to note that, due to the method of declustering, peaks occurring within 12-hours of a larger peak are not represented.

At the highest latitudes ($|\lambda| > 80°$), poleward of the dayside cusp, there is an occurrence maximum in the few hours about noon MLT, which persists over all timescales (1–60 min). For τ > 1 min, the maximum is much more sharply peaked for ramp changes than for RMS fluctuations, and as τ increases towards 60 min the MLT of the maximum occurs slightly later (towards 14 MLT). (Note that the timestamps and MLTs associated with each cluster peak of $|dB_h/dt|$ refers to the *end* of the n-minute period in question (from Equations (2) and (4)) but this is not sufficient to account for the apparent shift of the maximum towards the post-noon.) Analysis of the $\boldsymbol{R_1}$ distribution by Rogers et al. (2020) showed that these peaks near noon occur predominantly under northward IMF conditions during the summer months (i.e. under conditions of greatest dipole tilt angle), suggesting a possible relation to impulsive field line reconnection between the IMF and an 'overdraped' tail lobe (Wang et al., 2008; Milan et al., 2017; 2020; Crooker, 1992; Watanabe et al., 2005). The MLT distribution of occurrence probability at dayside cusp latitudes does not match the distributions of MIEs observed by Lanzerotti et al. (1991) and Kataoka et al. (2003) who reported a relatively flat distribution over 06–18 MLT with a minimum around 11 MLT, although these MIE distributions were not thresholded at a very high percentile. Nonetheless, the MIE amplitude distribution presented in Fig. 5d of (Kataoka et al., 2003) indicates perturbations approaching 400 nT (over ~5-15 min) in the 07–11 MLT period, which is not observed in the MLT profile of $P_{99.97}$ exceedances of Figure 2a. Such discrepancies indicate that it is less likely that MIEs (caused by TCVs) provide a significant contribution to the extremes of $|dB_h/dt|$ in this region.

At low latitudes $|\lambda|$ < 40°, for R_1 and R_{10}, and S_n for all n, the occurrence probabilities increase on the day-side at 07-16 MLT, although for $20° < |\lambda|$ < 43° the distribution is double-peaked with a dip in occurrence in the few hours around noon, creating a Y-shaped pattern most clearly discernible in the 1-min data (panels (a) or (e)). The distributions for R_{10} and R_{30} also have a night-time maximum in the period (19-03 MLT). Rogers et al. (2020) showed (in their Fig. 8) that approximately 25-70% of the R_1 peaks at these latitudes occurred at or within 30 minutes of a sudden commencement, as recorded with high confidence in IAGA bulletins (http://www.obsebre.es/en/rapid). However, the lower figure (25%) was associated with the largest occurrence probabilities near noon, suggesting that alternative or delayed driving processes may be contributing to the largest R_1 at these times.

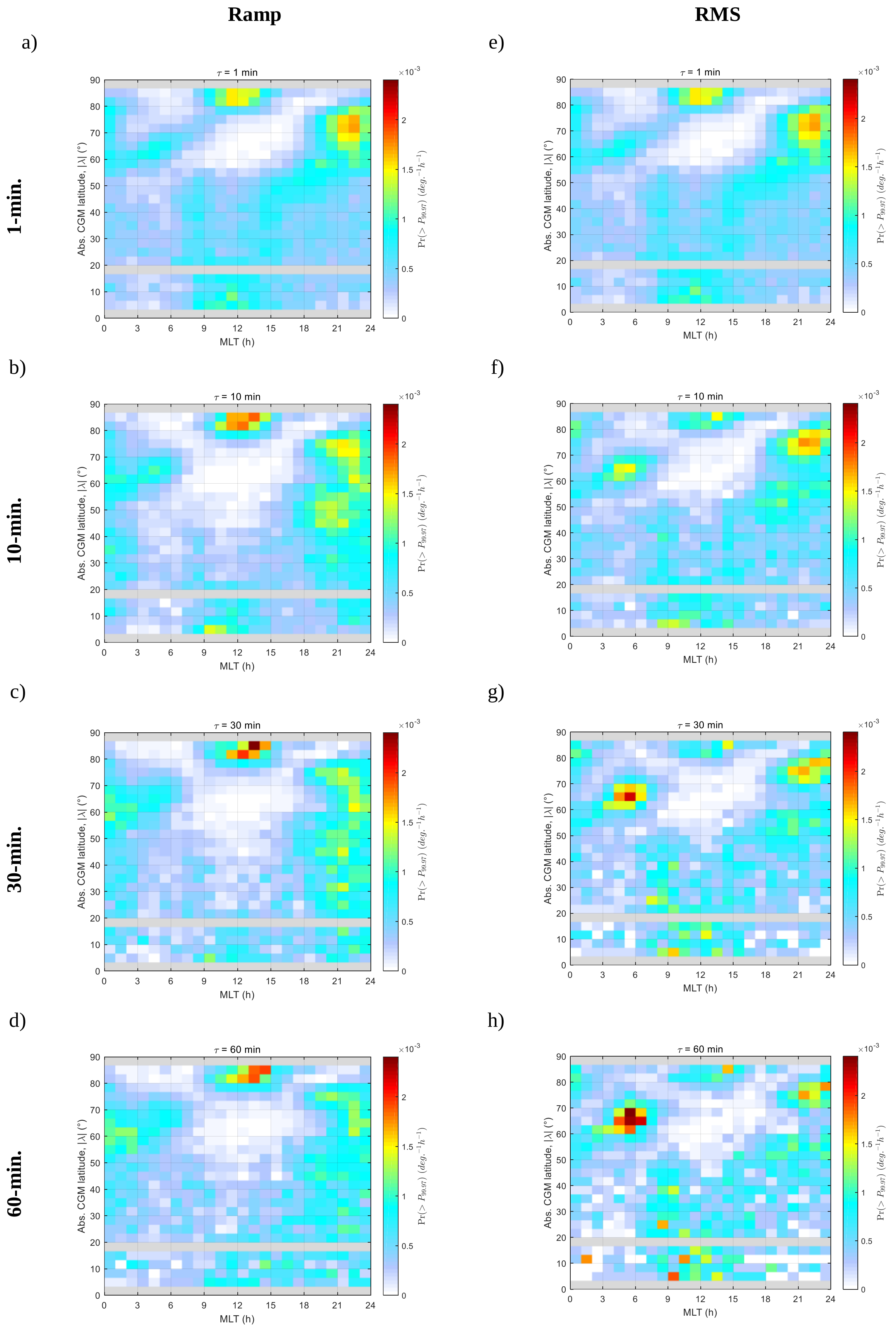

Figure 2. $Pr(|dB_h/dt| > P_{99.97})$ against CG latitude and MLT for (a) $\boldsymbol{R_1}$, (b), $\boldsymbol{R_{10}}$, (c) $\boldsymbol{R_{30}}$, (d) $\boldsymbol{R_{60}}$, (e) $\boldsymbol{S_1} (= \boldsymbol{R_1})$, (f), $\boldsymbol{S_{10}}$, (g) $\boldsymbol{S_{30}}$, (h) $\boldsymbol{S_{60}}$. Latitude bins with no magnetometers are coloured grey.

At auroral latitudes (60° < $|\lambda|$ < 75°) the occurrence probability $Pr(R_n > P_{99.97})$, is greatest in the few hours before local midnight (20–24 MLT) for all timescales. Substorm onsets occur most frequently in this MLT sector (Liou et al., 2001; Wang et al., 2005) so the increased prevalence of large R_n may be associated with the substorm expansion and recovery phases themselves, or with transient and localised MPEs, most of which occur within 30 min of a substorm onset. Engebretson et al. (2021) recently presented a statistical survey of MPEs at five Canadian sites (65–75°N geomagnetic) and their Fig. 4 showed that the distributions of MPE above a threshold of 6 nT/s (360 nT/min) (with a maximum of 37 nT/s (2220 nT/min)) contained a distribution in the range 02–06 MLT at only the lowest latitude station (65°N) whilst for the other four stations (71°N–75°N) a broad distribution of MPE occurrence was observed in the pre-midnight hours over 19–01 MLT. This observation is consistent with the MLT occurrence distributions shown in Figure 2a and b. The MLT of peak occurrence (in the pre-midnight hours) is approximately one hour earlier at the mid-latitudes associated with UK magnetometers (HAD, ESK and LER) (λ = 47.5°N–58°N). Freeman et al. (2019) observed that, for the same three UK sites, approximately 55% of R_1 peaks exceeding $P_{99.97}$ were associated with the expansion or recovery phase of a substorm.

A secondary peak of occurrence is observed in the dawn-noon sector. Some of these peaks below 70°N may be associated with MPEs since they are consistent with the 02-06 MLT distribution observed by Engebretson et al. (2021) for the station at 65°N geomagnetic, as noted above. However, this is also a region in which Pc5 pulsations are the dominant wave activity (e.g. Engebretson et al., 1998; Pulkkinen & Kataoka, 2006). The R_1 occurrence probabilities maximise at around 03 MLT at $|\lambda|$=60°, increasing to 12 MLT at $|\lambda|$ =80°, and similar patterns have been reported in the distribution of Pc5 wave power (compare, for example, Fig. 5 of Vennerstrøm (1999), Fig. 2 and 4b of Baker et al., 2003, or Fig. 1 of Weigel et al., 2002). The rate of occurrence for longer-period ramp changes, R_{10}, R_{30} and R_{60}, is suppressed in the latitude band $|\lambda|$ =70-77°, although this may be an effect of declustering where the peaks occur within 12 hours of larger amplitude fluctuations in the pre-midnight sector.

In contrast to the distribution of ramp changes, the occurrence patterns of large RMS fluctuations (Figure 2e-h) show that as the period, τ increases, the probability of occurrence $Pr(S_n > P_{99.97})$ in the auroral zone increases strongly in the dawn sector (03–07 MLT). A cursory inspection of magnetograms for the largest peaks of S_n indicated that many are indeed associated with ULF wave activity lasting tens of minutes (see, for example, Fig. 1c of (Rogers et al., 2020). To examine this further, an analysis of the probability of occurrence *vs* (month, MLT) is presented in Figure 3 for the 26 sites at latitudes λ = 60°–70°N. This figure shows that in the pre-midnight hours the frequency of occurrence is greatest near the equinoxes, when the geomagnetic field is more favourably oriented for reconnection with the IMF (Russell & McPherron, 1973; Zhao & Zong, 2012). However, for RMS fluctuations (Figure 3e–h), as τ increases from 1 min to 60 min, the greatest frequency of occurrence occurs on the dawn side (03–09 MLT). We also note, for both R_1 and S_1 distributions, a change in the locus of peak occurrence from 04–05 MLT near the summer solstice to 07–08 MLT near the winter solstice, which may be associated with changes in the position of the dawn terminator at these latitudes and the seasonal changes in the geometry of the geomagnetic field relative to the IMF. For τ >= 10 min, however, the frequency of occurrence in the winter months (December and January) is reduced relative to that for τ =1 min, in both R_n and S_n, and this also limits the time zones of occurrence in the late morning.

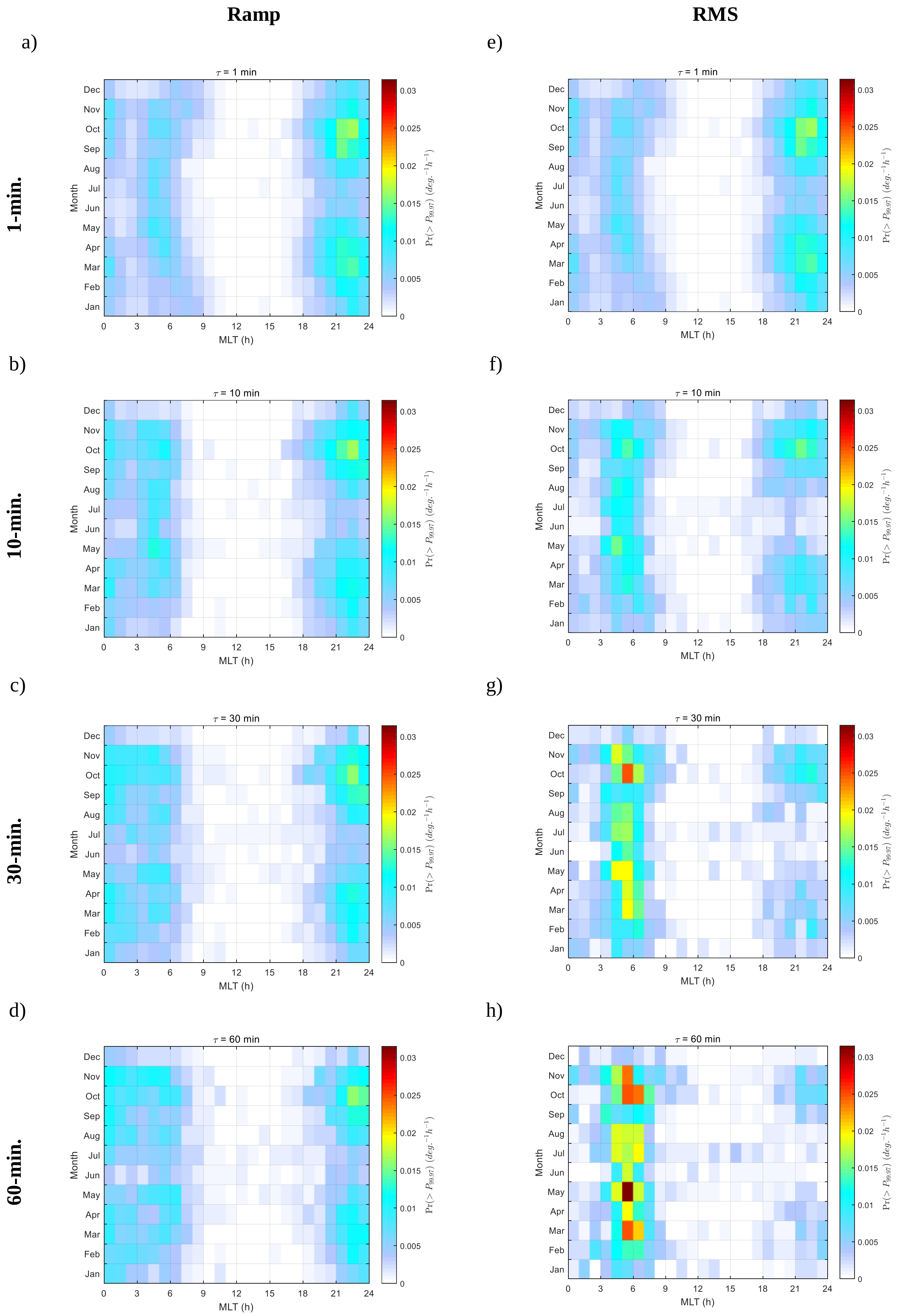

Figure 3. $Pr(|dB_h/dt| > P_{99.97})$ vs (MLT, month) for (a) $\boldsymbol{R_1}$, (b), $\boldsymbol{R_{10}}$, (c) $\boldsymbol{R_{30}}$, (d) $\boldsymbol{R_{60}}$, (e) $\boldsymbol{S_1}(= \boldsymbol{R_1})$, (f), $\boldsymbol{S_{10}}$, (g) $\boldsymbol{S_{30}}$, (h) $\boldsymbol{S_{60}}$ for stations between 60 – 70°N CG latitude.

4 The frequency and latitude dependence of R_n and S_n

4.1 Modelling the 99.97th percentile

We now develop a model for the geomagnetic fluctuation amplitude as a function of sampling frequency and geomagnetic latitude, first for the 99.97th percentile of $|dB_h/dt|$ and in Section 4.2 for predicted 100-year return level estimates. Figure 4 presents $P_{99.97}$ as a function of sampling frequency, $f_s = 1/\tau$ for a) R_n, and b) S_n at each of 125 magnetometer sites. The colour of each line indicates the absolute CG latitude of the site, $|\lambda|$, and the upper horizontal scale indicates the sampling period, τ. Since the axes are logarithmic in both $P_{99.97}$ and f_s, a straight line with gradient p would indicate the power-law relation, $P_{99.97}(f_s) \propto f_s^p$, but it is clear from the curvature of the lines, at least for ramp changes, that this is not an appropriate model and it is observed that the gradients, curvature and offset vary with latitude. This was modelled by fitting a quadratic function,

$$\boldsymbol{y} = p_1 \boldsymbol{x}^2 + p_2 \boldsymbol{x} + p_3 \tag{6}$$

where $\boldsymbol{y} = \log\left(P_{99.97}(\boldsymbol{f_s})\right)$ and $\boldsymbol{x} = \log(\boldsymbol{f_s})$.

a) b)

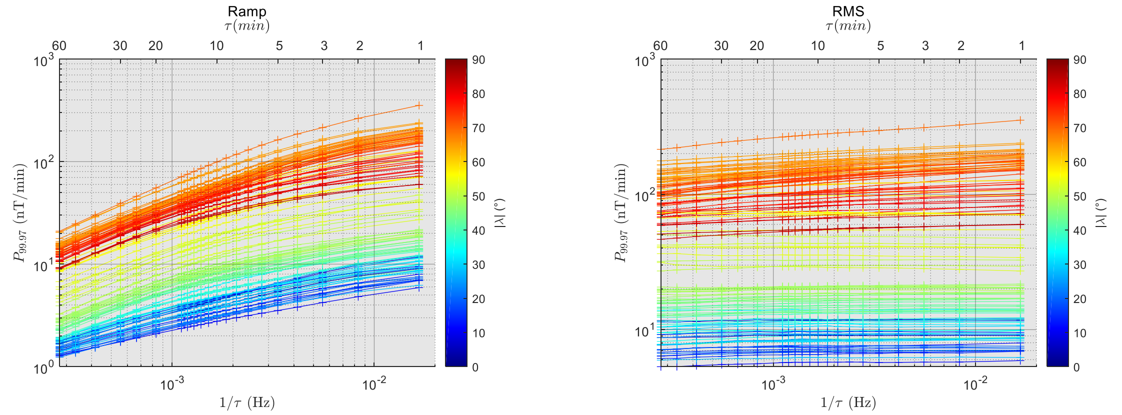

Figure 4. 99.97th percentiles of $|dB_h/dt|$ for a) Ramp changes (R_n) and b) RMS variation ($\boldsymbol{S_n}$) for 125 magnetometers, as a function of sampling frequency, $f_s = 1/\tau$, and coloured according to absolute CG latitude, $|\lambda|$.

The best-fit quadratic coefficient, p_1 linear coefficient, p_2, and constant term, p_3, are presented in Figure 5 as a function of λ. Here the error bars are 95% confidence intervals (CI) and, since the distributions are approximately symmetric about the equator ($\lambda = 0$), we have fitted smoothing splines (solid curves) using the *absolute* CG latitude as the dependent variable (i.e. fitting to $p_k(|\lambda|)$, for $k = 1,2,3$) and weighting each point by the inverse of the 95% CI. The constant terms (p_3) have broad maxima in the auroral zones, as expected from Figure 1. However, for ramp changes (Figure 5a), the linear and quadratic coefficients (p_2 and p_1) also show a strong dependence on $|\lambda|$. For RMS fluctuations (Figure 5b), the changes in p_2 and p_1 are much less significant. The smoothing spline fits to the coefficients thus provide a global model for the 99.97th percentiles of R_n, and S_n.

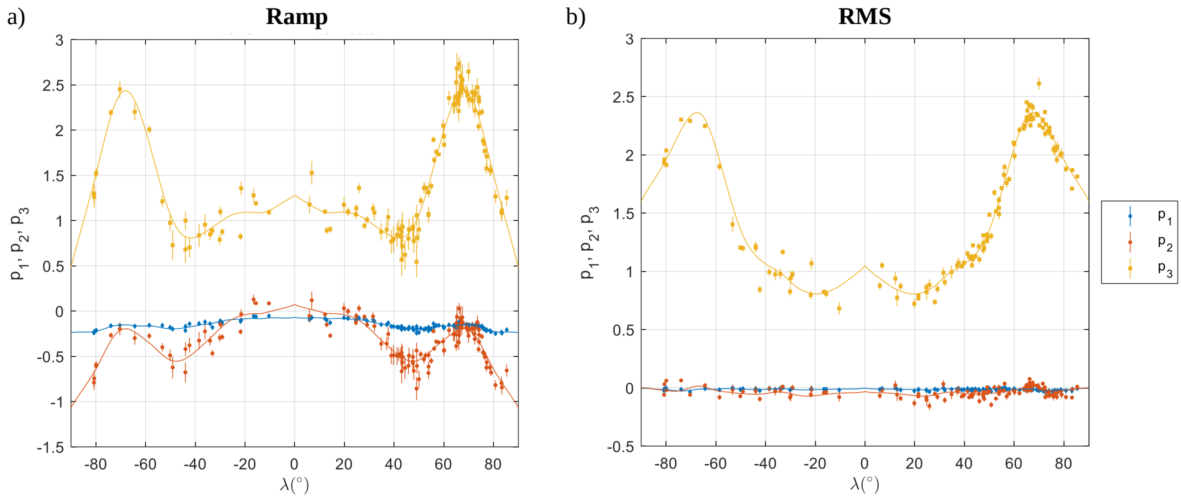

Figure 5. Coefficients of the polynomial (6) fitted to $\log P_{99.97}(\log f_s)$ at 125 magnetometers, for a) R_n, and b) S_n as a function of CG latitude. Error bars indicate 95% CIs. Solid lines indicate smoothed spline fits to $p_k(|\lambda|)$, for k=1,2,3 with points weighted by 1/CI. Units of p_k are (10 dB nT min^{-1} deg.$^{k-3}$).

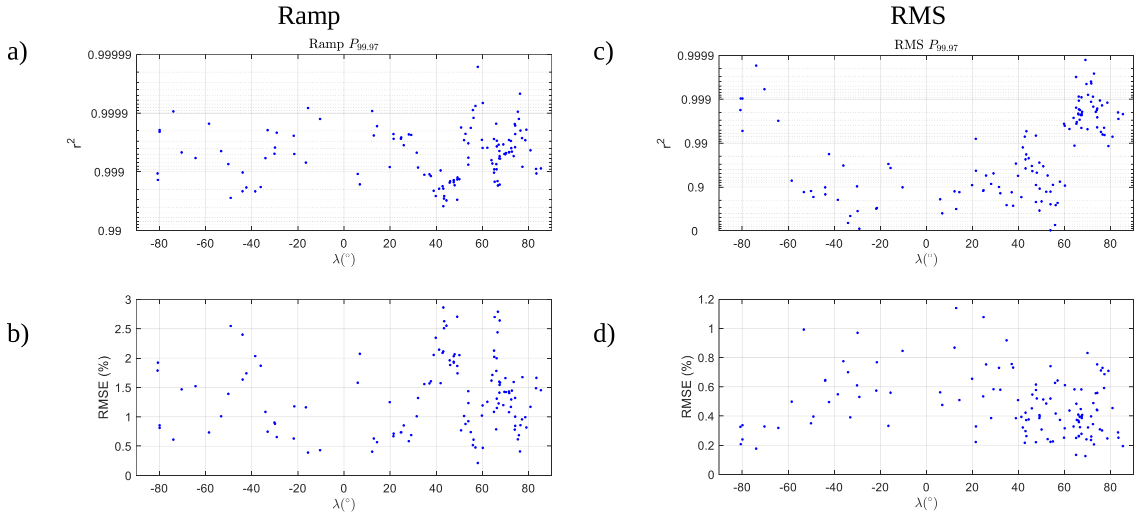

Figure 6. Goodness-of-fit metrics for the polynomial fit to $\log P_{99.97}(\log f_s)$ for (a, b) Ramp changes, and (c,d) RMS variations. Top panels (a,c) are coefficients of determination, r^2. Bottom panels (b,d) are the RMS of residuals.

The goodness of the quadratic fits at each magnetometer site are presented in Figure 6 for 99.97th percentiles of $\boldsymbol{R_n}$ (left panels, a and b) and $\boldsymbol{S_n}$ (right panels, c and d). Panels (a) and (c) present the coefficients of determination, r^2, whilst panels (b) and (d) present the RMS percentage error (i.e. the RMS value of $100\% \times (\widehat{\boldsymbol{P}}_{\mathbf{99.97}} - \boldsymbol{P}_{\mathbf{99.97}})/\boldsymbol{P}_{\mathbf{99.97}}$, where $\widehat{\boldsymbol{P}}_{\mathbf{99.97}}$ are the model estimates). The quadratic models for $\boldsymbol{R_n}$ fit well, with $r^2 > 0.99$ for all sites (see panel a), and RMS residuals less than 3%. The quadratic model for $\boldsymbol{S_n}$ fits well with $r^2 < 0.99$ (panel c), except at low-mid latitudes ($|\lambda| < 60°$) although for all sites the RMS of residuals is very low (< 1.2%).

4.2 Modelling return levels

Generalised Pareto (GP) distribution functions were fitted to exceedances of R_n above a $P_{99.97}$ threshold (after 12-h run-length declustering above the same threshold) independently for each magnetometer site. 100-year return levels of R_n were then determined from the GP distribution at a probability level equivalent to a 1-in-100 years of observations. A numerical method was used to determine a maximum likelihood estimate (MLE) for the return level with 95% confidence intervals determined from the (asymmetric) log-likelihood profile, as described in (Gilleland & Katz, 2016). This procedure was repeated for all 125 magnetometer sites and the results are plotted against $|\lambda|$ in Figure 7. Panels a, b, c and d, present 100-year return levels of R_n for *n* = 1, 10, 30, and 60 (minutes), respectively; points represent MLEs (coloured blue for southern hemisphere sites, black for northern hemisphere) with error bars indicating the 95% CI. The red curve in each panel is a smoothing-spline interpolation to the MLE values. In Figure 8 the interpolating spline curves are presented for return periods from 5 to 500 years.

The 100-year return levels for R_1 (Figure 7a) (1-minute ramp changes) are distinctly elevated for sites around $|\lambda| \cong$ 52–54° and reference to Figure 8 indicates that the latitude of this maximum decreases with increasing return period. This indicates that the extreme R_1 events (declustered threshold exceedances) that occur less frequently (i.e. with longer return periods) have greater amplitude and occur at lower absolute latitudes. This pattern of behaviour could indicate that largest and rarest auroral current fluctuations occur during substorm expansions associated with brightening auroral arcs at the equatorward edge of a greatly expanded auroral oval (i.e. following a large substorm growth phase). Over 10–60 minute timescales (Figure 7b to d) the peak near 53° is still present but less pronounced, and Figure 8b–d shows that it has similar or lower magnitude than the broad peak around $|\lambda| \cong$ 67° that was observed in the $P_{99.97}$ profiles (Figure 1a).

The same procedure of fitting GP distribution functions was used to determine extreme values for the RMS variation over *n*-minute periods, $\boldsymbol{S_n}$. Figure 9 presents the 100-year return levels and Figure 10 presents the smoothed-spline fits for 5–500 year return periods for the $\boldsymbol{S_n}$, again for periods of τ = 1, 10, 30, and 60 minutes, The shape of these distributions are very similar to those of the $\boldsymbol{R_n}$ fluctuations although the reduction in level with increasing τ is much less pronounced.

For both R_n and S_n metrics (Figure 8 and Figure 10, respectively) there is an increase in RLs towards the equator, potentially associated with activity in the equatorial electrojet current systems, and for return periods greater than 100 years there is a predicted increase in RL as latitude $|\lambda|$ increases above 74°, for τ = 1 and 10 min.

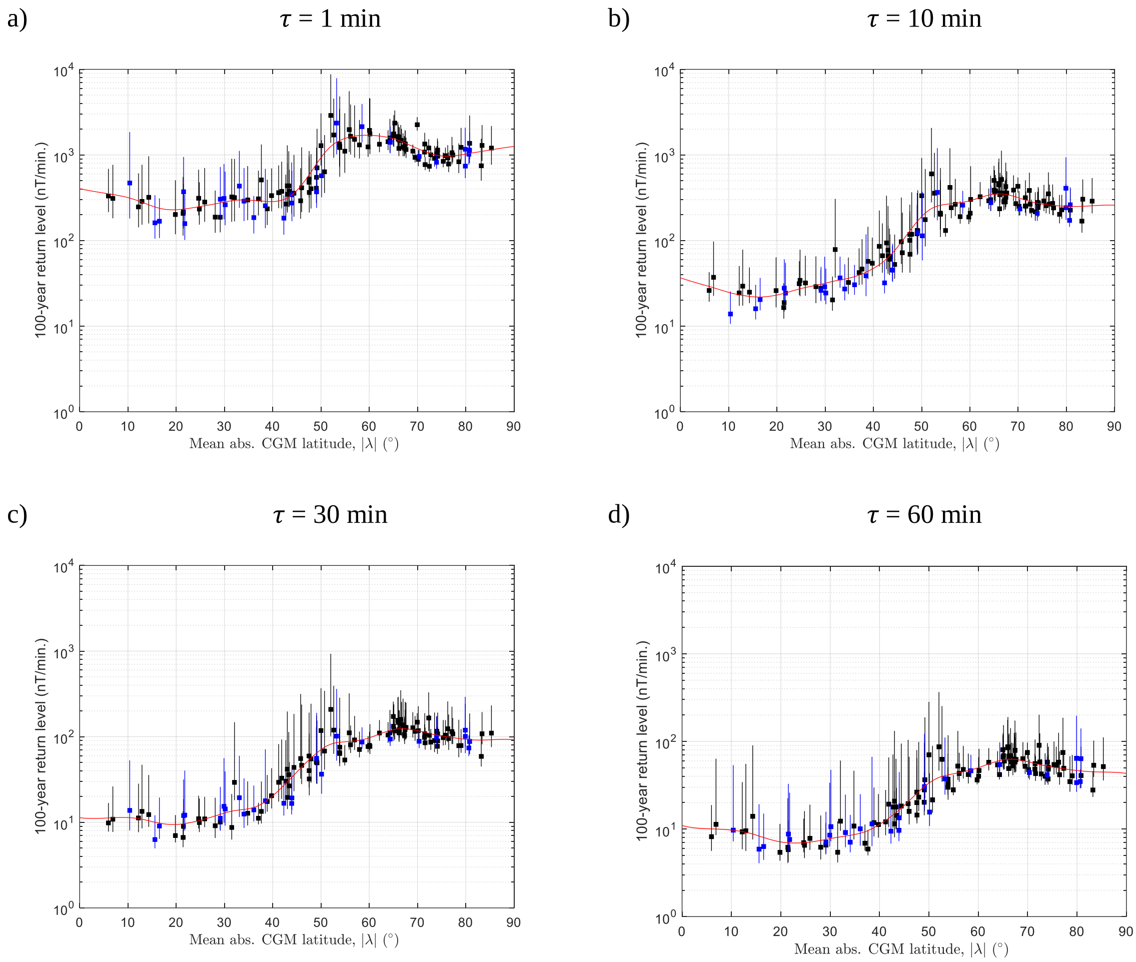

Figure 7. 100-year return levels (Max. likelihood estimates with 95% CI shown as error bars) for ramp changes ($\boldsymbol{R_n}$) estimated from GP distributions fitted above $P_{99.97}$. Black indicates NH sites, blue indicates SH. a) τ =1 min, b) τ = 10 min, c) τ = 30 min, and d) τ = 60 min. The red curves are smoothed spline fits to MLEs.

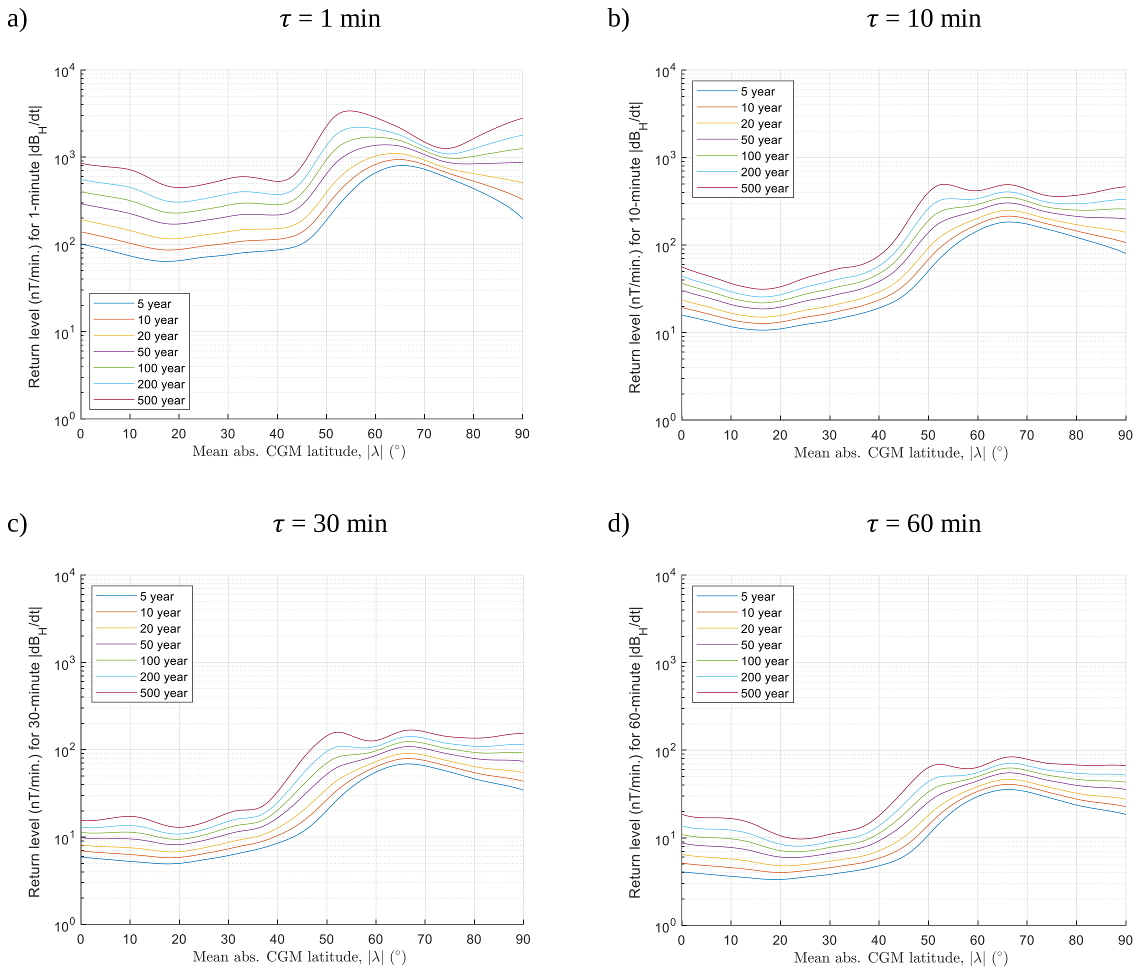

Figure 8. Smoothed spline fits to return levels of Ramp changes ($\boldsymbol{R_n}$), as shown by the red curve in Figure 7 (100-year Return Period), but repeated for a range of return periods. a) τ =1 min, b) τ = 10 min, c) τ = 30 min, and d) τ = 60 min.

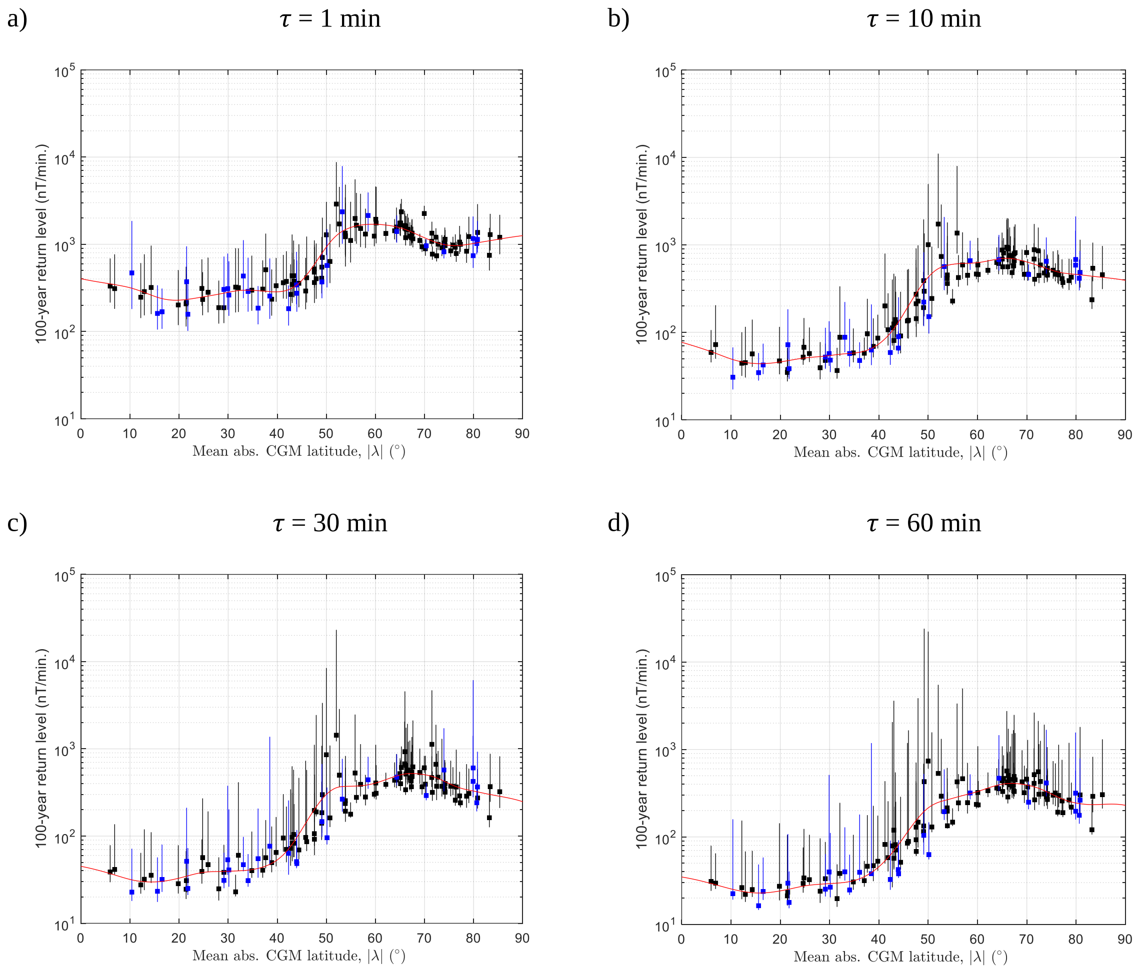

Figure 9. 100-year return levels (Max. likelihood estimates with 95% CI shown as error bars) for RMS variations ($\boldsymbol{S_n}$). Black indicates NH sites, blue indicates SH. a) τ =1 min, b) τ = 10 min, c) τ = 30 min, and d) τ = 60 min. The red curves are smoothed spline fits to MLEs.

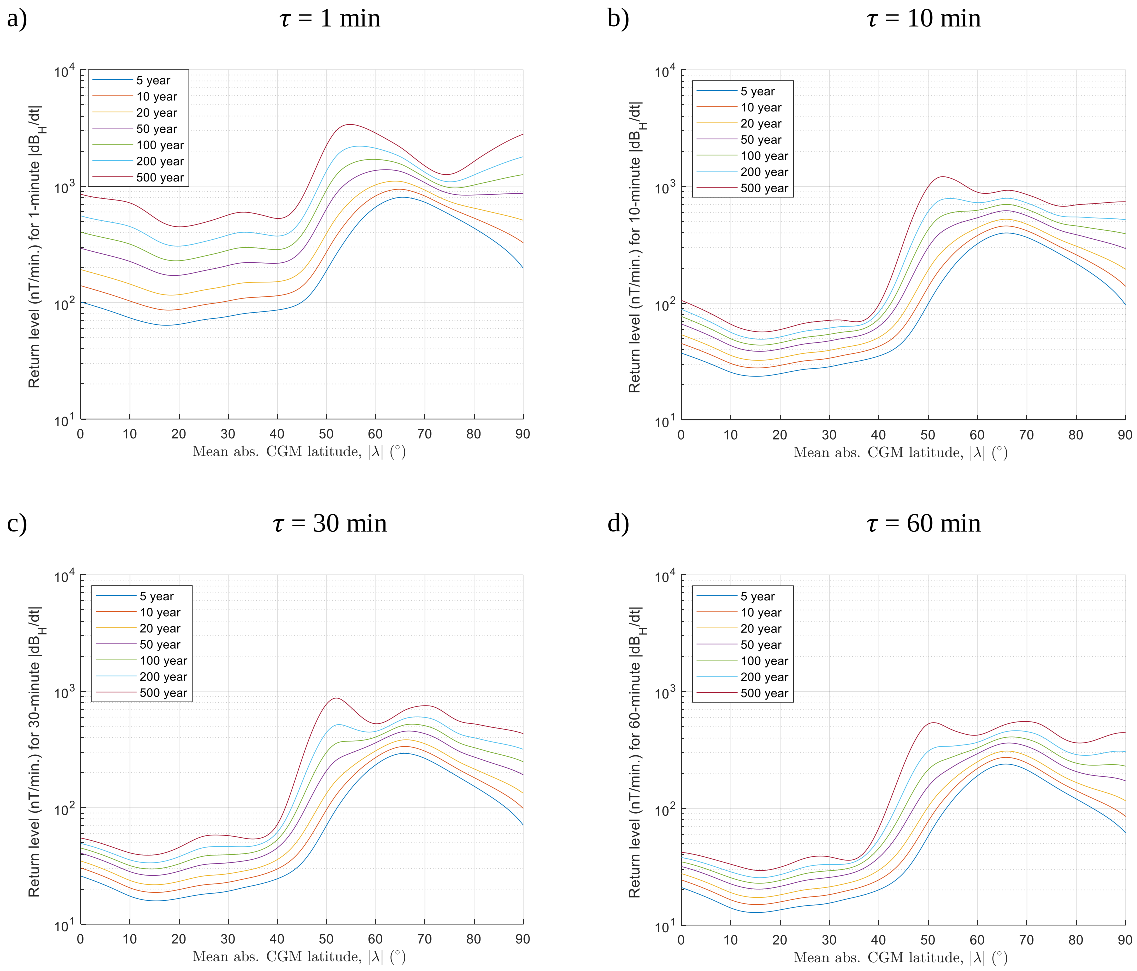

Figure 10. Smoothed spline fits to return levels of RMS variation ($\boldsymbol{S_n}$), as shown by the red curve in Figure 9 (100-year Return Period), but repeated for a range of return periods. a) τ =1 min, b) τ = 10 min, c) τ = 30 min, and d) τ = 60 min.

We now present models of the MLEs of 100-year return levels of R_n and S_n as functions of sampling frequency, f_s, and absolute CG latitude, $|\lambda|$, following the same procedure as for the $P_{99.97}$ levels developed in Section 4.1. Figure 11 presents 100-year RLs for a) $\boldsymbol{R_n}$ and b) $\boldsymbol{S_n}$, in the same format as Figure 4. The coefficients of the polynomials (6) fitted to the return levels are presented in Figure 12. The 95% CI of the fitted coefficients (error bars in Figure 12) are larger than for the $P_{99.97}$ model, but the profiles remain approximately symmetric about $\lambda =$ 0°. It is interesting to note for the ramp changes, $\boldsymbol{R_n}$, there is a pronounced change from positive to negative curvature as $|\lambda|$ increases, which can be seen in the profiles of Figure 11 and the change in quadratic coefficient, p_1, in Figure 12. For both $\boldsymbol{R_n}$ and $\boldsymbol{S_n}$, the gradients (or the linear coefficients, p_2) are significantly higher at lower latitude $|\lambda|$.

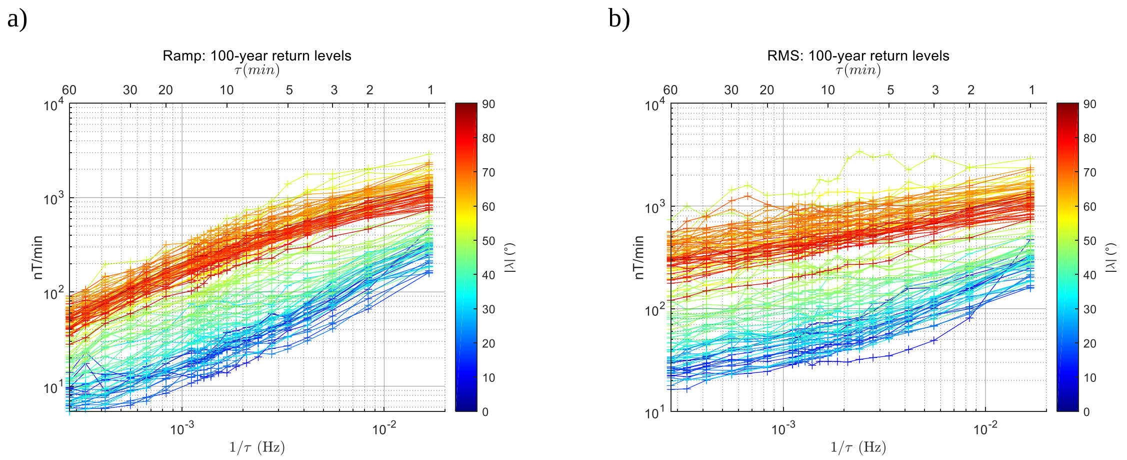

Figure 11. 100-year return levels for a) R_n, and b) S_n, for n = 1-60 min (top axis), plotted against the sampling frequency (bottom axis). MLE values are shown for all 125 magnetometer sites, coloured according to absolute geomagnetic latitude, $|\lambda|$.

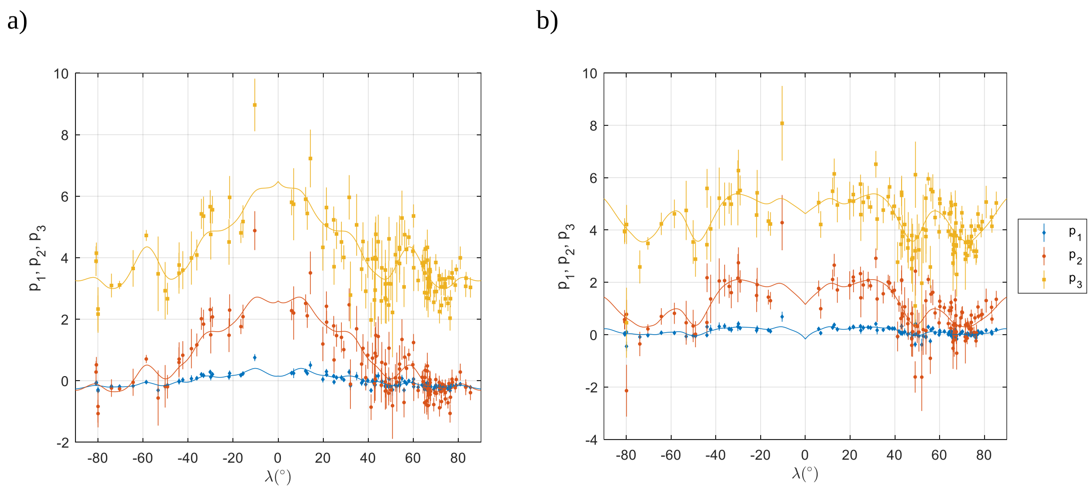

Figure 12. Coefficients of the polynomial (6) best fitted to 100-year return levels of $|dB_h/dt|$, presented in the same format as Figure 5. a) R_n, and b) S_n.

Figure 13 provides goodness-of-fit metrics for the polynomials (6) fitted to MLE of RL_{100}, presented in the same format as Figure 6. Not unexpectedly, RL_{100} shows greater variation from the polynomial model than $P_{99.97}$ (cf. Figure 6) but in the vast majority of cases the RMS errors are still less than 15% and have a coefficient of determination greater than 0.9.

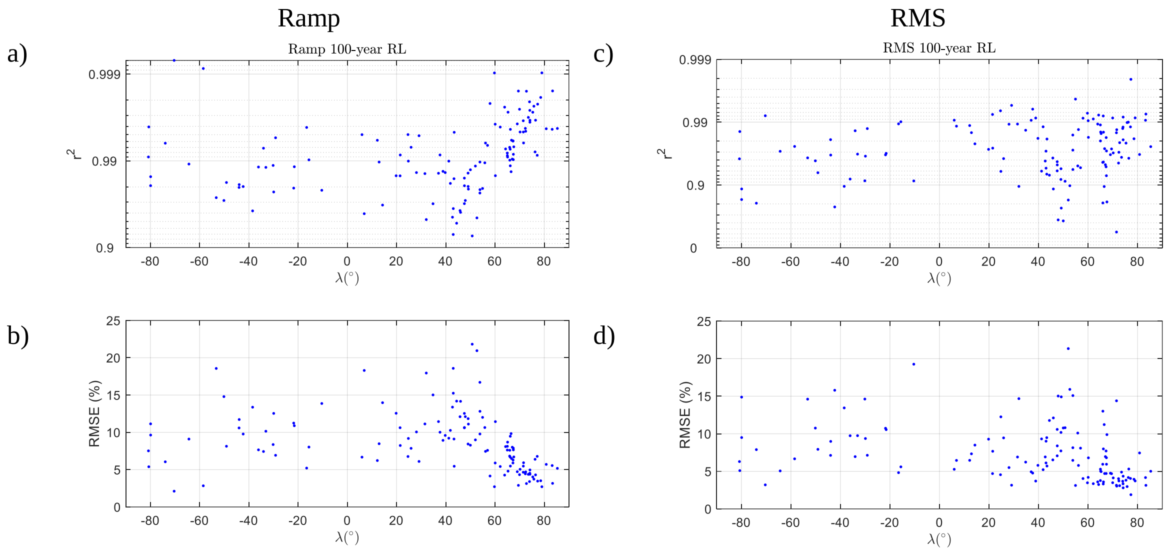

Figure 13. Goodness-of-fit metrics for the polynomial (6) fit to $\log RL_{100}(\log f_s)$ for (a,b) Ramp, and (c,d) RMS fluctuations. Top panels (a,c) are coefficients of determination, r^2. Bottom panels (b, d) are the RMS of residuals.

4.3 Predictions of extreme geoelectric fields in the UK

We shall now focus on the statistics for three UK magnetometer sites, HAD, ESK and LER. Figure 14 presents, for each site, the 99.97th percentiles of a) $\boldsymbol{R_n}$, and b) $\boldsymbol{S_n}$, and 100-year return levels for c) $\boldsymbol{R_n}$, and d) $\boldsymbol{S_n}$. For the ramp changes, $\boldsymbol{R_n}$ (Figure 14a and c) the frequency scale is extended up to 1 Hz using the 1-s cadence dataset. Whilst the length of the datasets differ for 1-s and 1-min data, the discontinuities in the $P_{99.97}$ curves (Figure 14a) at τ = 1 min are negligible, although a larger discontinuity arises from the RL estimates (Figure 14c). Statistics for $\boldsymbol{S_n}$ (Figure 14b and d) could not be extended to 1 Hz since they are defined from 1-min cadence measurements (Equation (4)), but they are presented here for τ = 1-60 min to illustrate that whilst the 99.97th percentile varies little with sample frequency (panel b), their 100-year RLs (panel d) have a much more significant frequency dependence, albeit with large 95% confidence intervals (illustrated by the shaded regions).

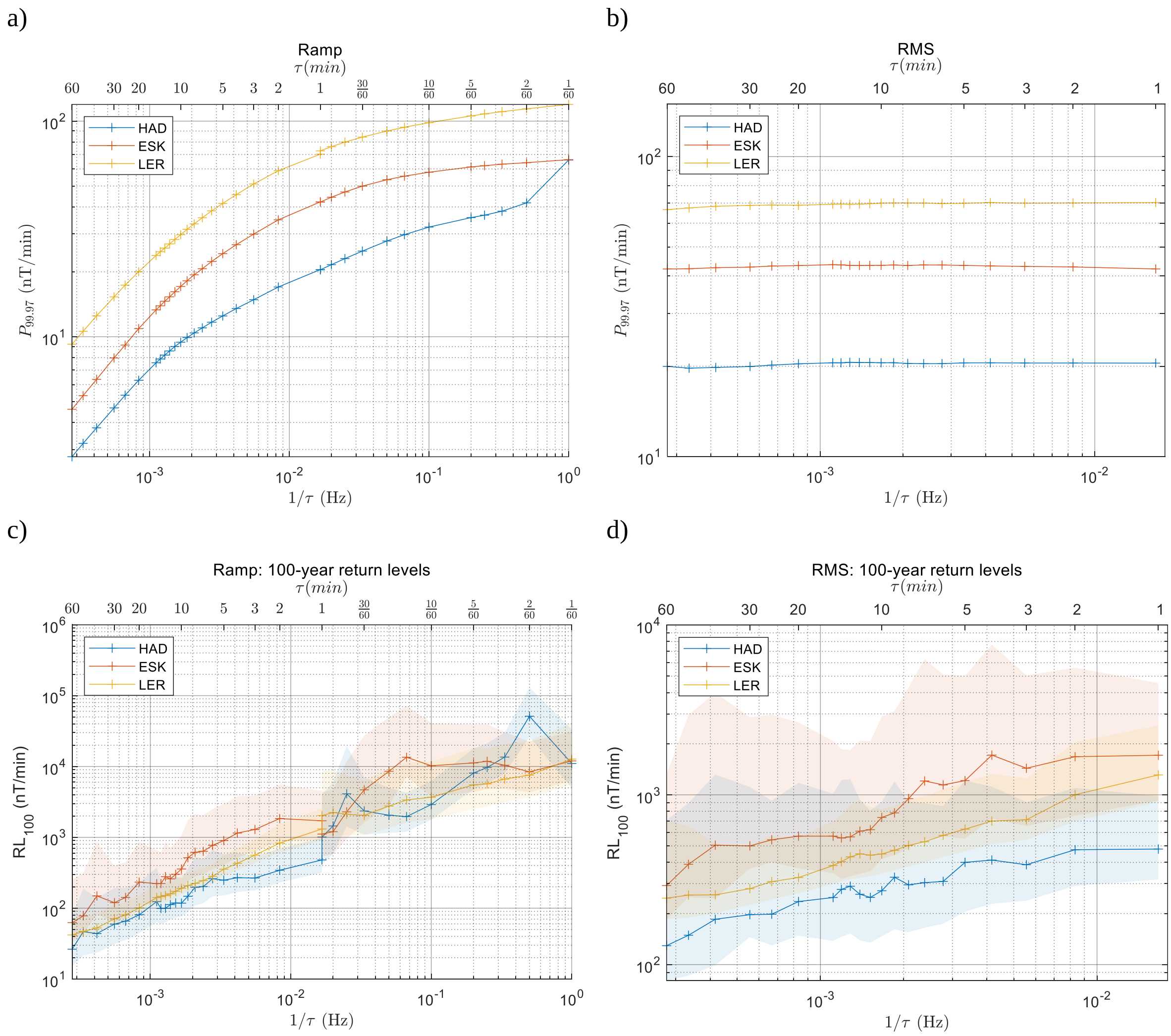

Figure 14. a) $P_{99.97}$ of $\boldsymbol{R_n}$, b) $P_{99.97}$ of $\boldsymbol{S_n}$, c) 100-year RLs of $\boldsymbol{R_n}$, and d) 100-year RL of $\boldsymbol{S_n}$, for three UK sites. RLs are maximum likelihood estimates, whilst the shaded regions indicate 95% confidence intervals.

To estimate the $P_{99.97}$ and 100-year return levels of the geoelectric field we applied the "plane wave" method, (Cagniard (1953); Pirjola (1982)) in which we consider an electromagnetic wave with frequency f (Hz) propagated vertically down along the z axis into the ground with uniform (or layered) conductivity, σ. For a wave polarised in the N-S plane, at the surface (z = 0) the magnetic field is

$$B_N = B_0 e^{i(2\pi f t - kz)} = B_0 e^{i2\pi f t} \qquad (7)$$

and the geoelectric field, E, induced at the surface ($z = 0$) will be

$$E_E = -\sqrt{\frac{2\pi f}{\mu_0 \sigma}} B_N \, e^{i\pi/4} \qquad (8)$$

in the east direction, where μ_0 is the permeability of free space, and σ is the conductivity of the ground. Equation (8) is known as the "basic equation of magnetotellurics" and is valid under the assumptions that the permeability,

$\mu = \mu_0$, permittivity, $\epsilon \ll \sigma/2\pi f$, and the conductivity of the air above the surface is negligible. Considering an additional orthogonal component of the magnetic field B_E, we may write (8) more generally as

$$\begin{pmatrix} E_N \\ E_E \end{pmatrix} = \begin{pmatrix} 0 & Z \\ -Z & 0 \end{pmatrix} \begin{pmatrix} B_N \\ B_E \end{pmatrix} \tag{9}$$

or in vector notation

$$\boldsymbol{E}(f) = \boldsymbol{Z}(f)\boldsymbol{B}(f) \tag{10}$$

where

$$Z = \sqrt{\frac{2\pi f}{\mu_0 \sigma}}\, e^{\frac{i\pi}{4}} \tag{11}$$

is the ‘magnetotelluric impedance’ (units of (V/km)/nT), which is related to the electromagnetic wave impedance by a factor of μ_0. In the analysis that follows, we shall substitute the directly measured MT transfer functions $\boldsymbol{Z}(f)$ measured at the three UK geomagnetic observatory sites. The apparent resistivity for each of the four components of the observed $\boldsymbol{Z}$**,** is derived simply from (11) as

$$\rho_{a(ij)} = \frac{\mu_0}{2\pi f} \left| Z_{ij} \right|^2 \tag{12}$$

where ($Z_{ij} = Z_{xx}, Z_{xy}, Z_{yx}, Z_{yy}$), and presented for each site in Figure 15 (panels a, c, e) together with the phases of Z_{ij} (panels b, d and f). This representation, familiar to geophysicists, highlights differences from the uniform half-space response (9) which would be flat in ρ_a and with uniform 45° phase. The apparent resistivity of the ground differs greatly between sites as is expected from the very different geological settings that give rise to the electrical response.

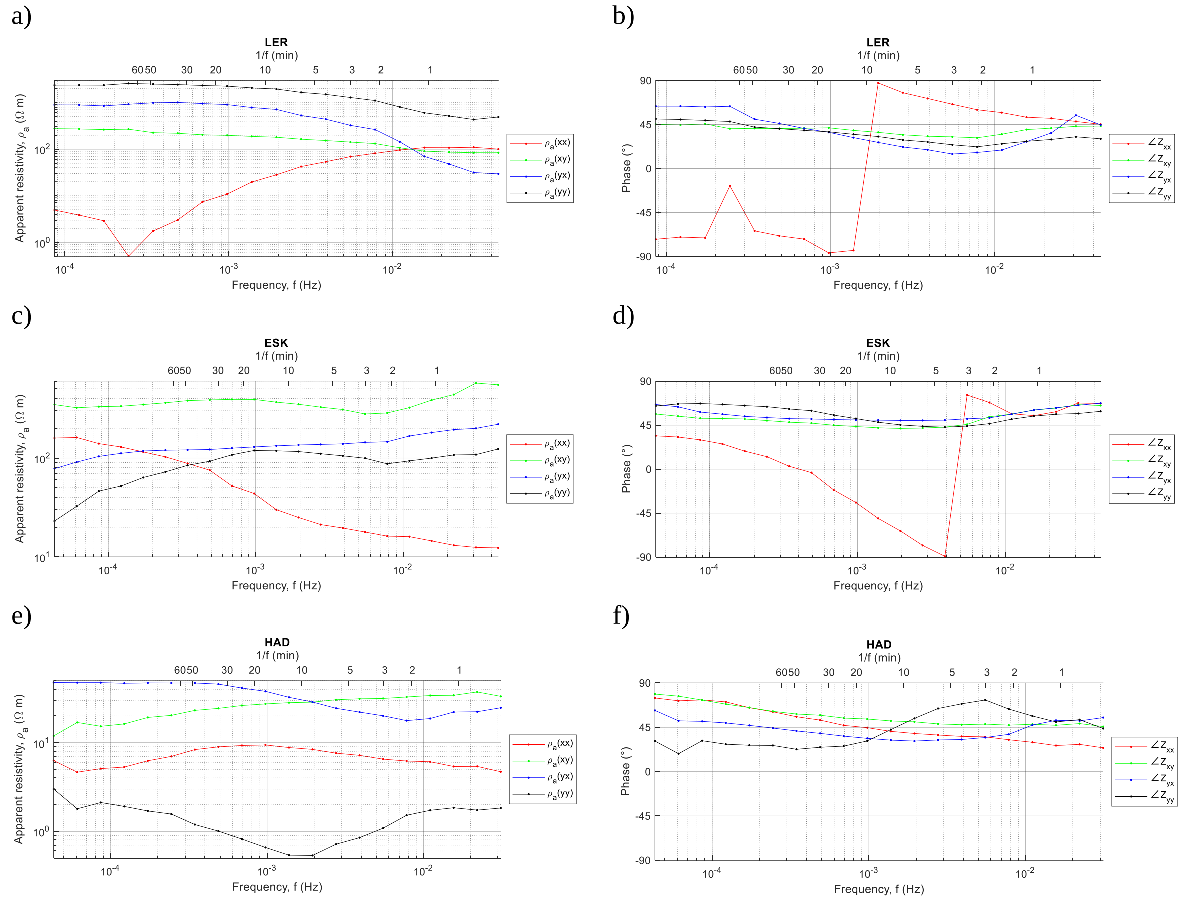

Figure 15. Apparent resistivity and phase of $\boldsymbol{Z}$, determined empirically for a-b) LER, c-d) ESK, and e-f) HAD magnetometers. Panels (a, c, e) show the apparent resistivity, and panels (b, d, f) show the phase.

For each site, the off-diagonal components $\rho_{a(xy)}$ *and* $\rho_{a(yx)}$ are not of equal magnitude, which indicates that the MT transfer function introduces 'directional anisotropy' (i.e. from Equation (10), $|E_N| \neq |E_E|$ when $|B_N| = |B_E|$). The diagonal terms $\rho_{a(xx)}$ *and* $\rho_{a(yy)}$ are non-zero (notably for Lerwick), suggesting some deviation from the simple half-space model (i.e. measurements imply a fully three-dimensional distribution of electrical resistivity).

Noting from (7) that

$$\frac{dB_N}{dt} = i2\pi f B_N \tag{13}$$

and similarly for B_E, we may estimate the geoelectric field from the rate-of-change of the magnetic field:

$$\boldsymbol{E}(f) = \frac{1}{i2\pi f}\boldsymbol{Z}(f)\begin{pmatrix}\frac{dB_N}{dt}(f)\\ \frac{dB_E}{dt}(f)\end{pmatrix} \tag{14}$$

In the ideal case of homogenous ground conductivity, equations (14) and (11) indicate that the spectrum of $|E|$ is proportional to $f^{-0.5}$ times the spectrum of $|dB/dt|$ (i.e. it is low-pass filtered).

To estimate the amplitude of the geoelectric field expected to result from the 99.97th percentile of R_n for a range of frequencies, we modelled the waveform as a vertically propagated sinusoid $B_0 \sin(2\pi f)$ with amplitude $B_0 = \tau P_{99.97}/2$ and frequency $f = 1/(2\tau)$. This required a linear interpolation of the $P_{99.97}$ (Figure 14a) to frequencies recorded in the MT transfer function at each site (Figure 15). The resulting estimates of the magnitude $|E| = \sqrt{E_N^2 + E_E^2}$ from Equation (10) are presented in Figure 16a where circles represent *B*-field fluctuations confined to the N-S plane ($|B_N| = B_0$; $B_E = 0$) and asterisks represent *B*-field fluctuations in the E-W plane ($B_N = 0$; $|B_E| = B_0$). The two polarisations yield *E*-fields that differ in magnitude by a factor of up to 2 because the MT transfer function is not directionally isotropic and the ground impedance depends on all three coordinates (x, y, z). At each UK site, exceedances of $P_{99.97}$, after declustering, occurred on average every 0.1 to 0.35 years over the range τ = 1 to 60 min, and so should be considered as large, but not extreme values. Figure 16b presents the *E*-field magnitude for sinusoids with peak-to-peak amplitude ($2B_0$) equal to the 100-year return levels, $\boldsymbol{R_n}$ (from Figure 14c).

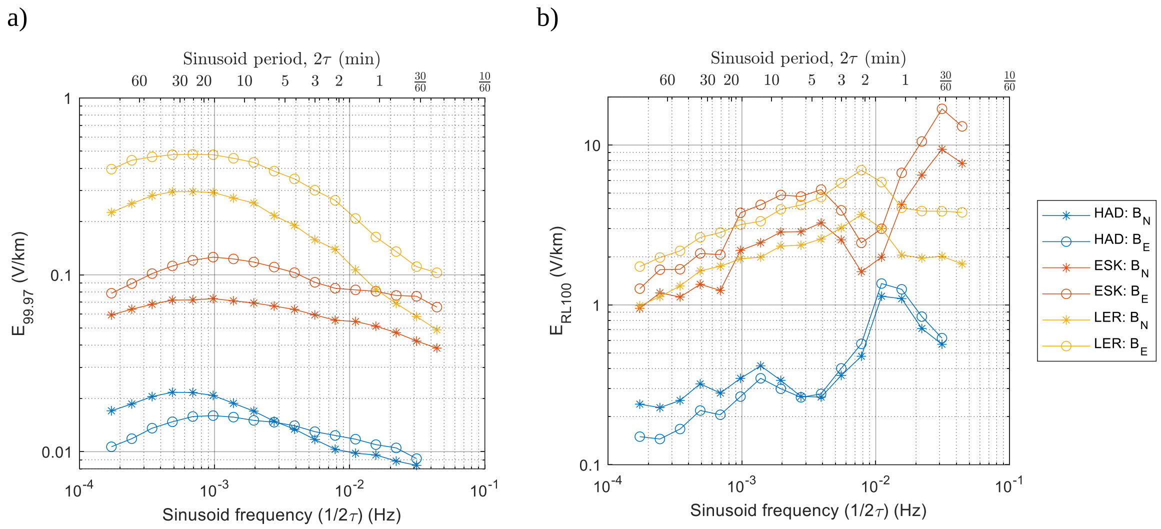

Figure 16. a) 99.97th percentile and b) 100-year RL of |*E*| at three UK sites. Circles indicate fields modelled with sinusoidal *B*-field in the N-S plane, asterisks are for *B* in the E-W plane.

To put these values in context, an *E* field of 1–2 V/km over large distances can, depending on the grid topology, produce GIC that saturates the steel core of a high-voltage transformer, which may lead to heating and potential failure of core components and the introduction of harmonics in the power system (Barnes et al., 1991). Winter et al. (2017) estimated the *E* field at UK latitudes associated with the 1859 storm – the largest geomagnetic storm on record (Carrington, 1859; Cliver & Dietrich, 2013) – to be approximately 9 V/km, and it is estimated that the nine-hour Hydro-Québec electricity blackout of March 1989 resulted from *E* fields of about 10 V/km (Barnes et al., 1991).

The predicted frequency dependences for the 99.97th percentile of $|E|$ (denoted $E_{99.97}$) take a very different form to those for the 100-year return levels (denoted E_{RL100}): E-field amplitudes at the 99.97th percentile (occurring several times a year) are greatest for sinusoid periods of approximately 20 min, whilst 1/100 year events have greatest amplitude for periods between 30 s and 2 min. The observation that 100-year RL predictions vary greatly with sinusoid frequency has important implications when comparing and contrasting statistical studies evaluating extremes of |*E*| which may have been based on different sinusoid frequencies.

Model estimates of the E field based on single-frequency components of the geomagnetic fluctuation have been reported by several authors (Beggan et al., 2013; Beggan, 2015; Bedrosian and Love, 2015; Love et al., 2016b). Love et al. (2016b) examined the amplitude of 4-min period sinusoids fitted to geomagnetic measurements (over sliding 10-min windows) and estimated extreme E-field amplitudes using empirical MT transfer functions at sites in the contiguous USA ($\lambda \cong$ 40–60°N). Only at the northern limit, in the northern mid-west states, did they find E_{RL100} exceeding 3 V/km, which is similar to the 3-5 V/km predicted in Figure 16 for LER (λ = 58°N) for a 4-min sinusoid period. However, direct comparisons between sites cannot be made without considering differences in the surface impedance and its gradients. Bedrosian and Love (2015) illustrated this point by simulating the E fields generated by sinusoids with 10-, 100-, and 1000-s periods using MT transfer functions from the EarthScope MT array in the Midwest USA and showed that a constant-amplitude B_0 = 500 nT, 100-s period B field would induce |E| of 2.7 V/km, averaged across all sites, but with values ranging from 0.15 to 16.8 V/km depending on site. Similarly, Pulkkinen et al. (2012), by extrapolating a log-normal distribution of 10-s field data from 23 European sites (55°-75°N geomagnetic), predicted E_{RL100} ranging from 5V/km with a high-conductivity ground model, to 20 V/km for poor-conductivity ground. Beggan et al. (2013) and Beggan (2015) also modelled the extreme E-field in the UK based on a conductivity model and B-fields modelled as sinusoids with periods, T, of 2, 10 and 30 minutes and amplitudes based on the 30-, 100-, and 200-year return levels of 1-min dB_h/dt predicted by Thomson et al. (2011). The 2-min E_{RL100} prediction of Beggan et al. (2013) shown in their Fig. 6 (middle column) shows not only the high level of localisation of the E field intensity, ranging from around 2 to 7 V/km, but also the importance of the direction of the inducing B-field (whether N-S or E-W aligned) for some locations. We intend to report further on the importance of directionality in extreme dB_h/dt statistics in a forthcoming publication.

There are, of course, limitations to 'narrowband' models of geomagnetic events since, in practice, fluctuations will be broadband in nature and the frequency spectrum of any individual geomagnetic event will be unique. We have noted that many of the extreme events (exceeding $P_{99.97}$) identified in our dataset occur simultaneously (within hours of each other) over a wide range of timescales (or frequencies), but our results should not be used to infer a frequency spectrum of B or E fields for any given extreme geomagnetic event. For this information the reader may refer to several studies of extreme values that have taken the approach of analysing the E field produced during rare and intense geomagnetic storm periods and in some cases scaling up their effect to simulate 100-year return levels (e.g. Ngwira et al., 2013; Pulkkinen et al. 2012; Lotz & Danskin, 2017).

5 Conclusion

The importance of ULF waves in driving extreme geoelectric fields and GICs has received a great deal of interest in recent years (Hartinger et al., 2020; Belakhovsky et al. 2019; Heynes et al. 2020; Pulkkinen & Kataoka, 2006) and there is a need for better understanding of the frequency dependence of the B and E field fluctuations driving GICs (e.g. Pulkkinen et al., 2017). Most previous statistical climatological studies of extreme values for E and dB_h/dt have been based on sampling at just one or two frequencies. In this paper, however, we have presented statistics of large ($P_{99.97}$) and extreme (e.g. 1/100-year) values for $|dB_h/dt|$ on a wide range of timescales, τ, from 1 to 60 min. At latitudes above the dayside cusp (λ > 80°), for example, we find that occurrences of $|dB_h/dt|$ ramp changes above $P_{99.97}$ become tightly clustered in the few hours about local noon, and the effect is greatest for longer timescales ($\tau \geq 30$ min). We have contrasted the statistics of ramp changes with those of the RMS of 1-min fluctuations over the same range of timescales and find, in particular, that in the auroral zone, for $\tau > 10$ min the MLT of greatest occurrence of large RMS variation is from dawn to noon, indicative of strong ULF wave activity in this local time sector. The frequency $(1/\tau)$ dependences (for both ramp changes and RMS variations) are found to be not a simple power law, but are well modelled by quadratic functions whose three coefficients vary predictably with geomagnetic latitude.

For three UK locations we extended the data set to 1 Hz sampling frequency and, using a plane wave approximation and measured MT transfer functions, we derived the frequency dependence of the 99.97th percentile and 100-year return levels of the geoelectric field, *E* at those sites. For events occurring several times a year (at the 99.97th percentile) the induced *E* fields were greatest for fluctuations of 20-min period, whilst the 1-in-100-year return levels were greatest for 0.5–2 min period fluctuations.

These statistics may be useful when inferring the likely extremes of $|dB_h/dt|$ or *E* over a wide frequency range based on studies that used a single sampling cadence. The distributions of extreme occurrence rates with latitude, local time and season may also improve our understanding of the main ionospheric and magnetospheric drivers of GICs.

IAGA code	Location	Geodetic latitude (°N)	Geodetic longitude (°E)	Mean Corrected Geomagnetic latitude (°N)	Mean Corrected Geomagnetic longitude (°E)
ABG	Alibag, India	18.62	72.87	12.19	145.59
ABK	Abisko, Sweden	68.35	18.82	65.29	101.98
AMS	Martin-de-Viviès, Amsterdam I.	-37.8	77.57	-49.10	138.76
AND	Andenes, Norway	69.3	16.03	66.53	99.89
API	Apia, Samoa	-13.8	188.22	-15.59	-97.20
ASC	Ascension Island	-7.95	345.62	-10.37	56.47
ASP	Alice Springs, Australia	-23.77	133.88	-34.06	-152.63
ATU	Attu, India	67.93	306.43	74.19	38.37
BDV	Budkov, Czechia	49.07	14.02	44.40	89.37
BEL	Belsk, Poland	51.83	20.8	47.55	96.06
BFE	Brorfelde, Denmark	55.62	11.67	52.03	89.51
BJN	Bjørnøya, Svalbard	74.5	19.2	71.47	107.94
BLC	Baker Lake, Canada	64.33	263.97	74.01	-32.85
BMT	Beijing Ming Tombs, China	40.3	116.2	34.81	-170.72
BOU	Boulder, USA	40.13	254.77	49.04	-40.52
BRW	Utqiaġvik, Alaska, USA	71.3	203.25	69.95	-109.37
BSL	Bay St Louis, USA	30.35	270.37	41.23	-19.39
CBB	Cambridge Bay, Canada	69.1	255	77.32	-51.99
CBI	Chichi-jima, Japan	27.15	142.3	19.83	-146.53
CDC	Cape Dorset, Canada	64.2	283.4	73.54	2.26
CHD	Chokurdakh, Russia	70.62	147.89	65.11	-146.75
CLF	Chambon-la-forêt, France	48.02	2.27	43.42	79.46
CMO	College, Alaska, USA	64.87	212.14	64.99	-96.46
CNB	Canberra, Australia	-34.1	150.7	-43.93	-131.74
CSY	Casey, Antarctica	-66.28	110.53	-80.79	156.40
CTA	Charters Towers, Australia	-20.1	146.3	-29.15	-139.40
CZT	Port-Alfred, Crozet Is.	-46.43	51.87	-53.25	106.05
DAW	Dawson City, Canada	64.05	220.89	65.94	-86.42
DLR	Del Rio, USA	29.49	259.08	38.87	-34.04
DMH	Danmarkshavn, Greenland	76.77	341.37	77.15	85.12
DOU	Dourbes, Belgium	50.1	4.6	45.79	81.68
DRV	Dumont d'Urville, Antarctica	-66.67	140.01	-80.65	-124.47
DRW	Darwin, Australia	-12.4	130.9	-21.53	-156.74
ESK	**Eskdalemuir, Scotland, UK**	**55.32**	**356.8**	**52.65**	**77.41**
EWA	Ewa Beach, Hawaii, USA	21.32	202	21.43	-90.00
EYR	Eyrewell, New Zealand	-43.4	172.4	-50.13	-103.35
FCC	Fort Churchill, Canada	58.76	265.92	69.04	-28.23
FHB	Paamiut, Greenland	62	310.32	67.63	39.03
FMC	Fort McMurray, Canada	56.66	248.79	64.29	-51.11
FRD	Fredericksburg, USA	38.2	282.63	49.08	-2.14
FRN	Fresno, USA	37.1	240.3	43.05	-56.30
FSP	Fort Simpson, Canada	61.76	238.77	67.34	-66.07
FUR	Fürstenfeldbruck, Germany	48.17	11.28	43.33	86.85
FYU	Fort Yukon, Canada	66.57	214.7	67.28	-93.86
GDH	Qeqertarsuaq, Greenland	69.25	306.47	75.79	40.39
GHB	Nuuk, Greenland	64.17	308.27	70.18	37.83
GIM	Gillam, Canada	56.38	265.36	66.24	-27.15
GLN	Glenlea, Canada	49.65	262.88	60.06	-31.75
GNA	Gnangara, Australia	-31.8	116	-43.98	-172.78
GUA	Guam	13.59	144.87	5.96	-144.13
GUI	Güímar, Canary Is.	28.32	343.57	12.91	60.66
HAD	**Hartland, England, UK**	**50.98**	**355.52**	**47.55**	**74.87**
HBK	Hartebeesthoek, S. Africa	-25.88	27.71	-36.09	94.69
HER	Hermanus, S. Africa	-34.43	19.23	-42.31	82.28
HLP	Hel, Poland	54.61	18.82	50.74	94.98
HON	Honolulu, Hawaii, USA	21.32	202	21.50	-90.13
HRB	Hurbanovo, Slovakia	47.86	18.19	43.03	92.69
HRN	Hornsund, Svalbard	77	15.6	74.18	108.69
HTY	Hatizyo, Japan	33.12	139.8	25.90	-148.91
IQA	Iqaluit, Canada	63.75	291.48	72.32	15.00
IRT	Irkoutsk, Russia	52.17	104.45	47.58	177.74
KAG	Kagoshima, Japan	31.48	130.72	24.80	-157.02
KAK	Kakioka, Japan	36.23	140.18	29.13	-148.35
KDU	Kakadu, Australia	-12.69	132.47	-21.78	-155.03
KNY	Kanoya, Japan	31.42	130.88	24.64	-157.04
KUV	Kullorsuaq, Greenland	74.57	302.82	80.81	42.87
LER	**Lerwick, Scotland, UK**	**60.13**	**358.82**	**57.97**	**81.13**
LOV	Lovoe, Sweden	59.35	17.83	55.85	96.36
LRM	Learmonth, Australia	-22.22	114.1	-33.09	-174.14

LRV	Leirvogur, Iceland	64.18	338.3	65.02	67.19
LYR	Longyearbyen, Svalbard	78.2	15.83	75.34	110.77
MAB	Manhay, Belgium	50.3	5.68	46.00	82.63
MAW	Mawson Station, Antarctica	-67.61	62.88	-70.35	90.48
MCM	McMurdo Station, Antarctica	-77.85	166.67	-79.91	-31.86
MCQ	Macquarie Island	-54.5	158.95	-64.34	-111.60
MEA	Meanook, Canada	54.62	246.65	62.12	-54.58
MGD	Magadan, Russia	59.97	150.86	53.89	-140.23
MMB	Memambetsu, Japan	43.91	144.19	37.04	-144.39
MSR	Moshiri, Japan	44.37	142.27	37.65	-145.93
MUT	Muntinlupa, Philippines	14.37	121.02	6.87	-167.21
NAL	Ny Ålesund, Svalbard	78.92	11.95	76.27	109.73
NAQ	Narsarsuaq, Greenland	61.16	314.56	66.20	43.47
NCK	Nagycenk, Hungary	47.63	16.72	42.72	91.38
NEW	Newport, USA	48.27	242.88	54.94	-56.65
NGK	Niemegk, Germany	52.07	12.68	47.94	89.00
NUR	Nurmijärvi, Finland	60.5	24.65	56.96	102.10
ONW	Onagawa, Japan	38.43	141.47	31.52	-146.75
OTT	Ottawa, Canada	45.4	284.45	56.13	0.83
PAF	Port-aux-Français, Kerguelen Is	-49.35	70.26	-58.51	122.00
PBQ	Poste-de-la-Baleine, Canada	55.28	282.26	66.00	-1.68
PGC	Pangnirtung, Canada	66.1	294.2	74.14	20.10
PHU	Phú Thủy, Vietnam	21.03	105.95	14.31	178.11
PIN	Pinawa, Canada	50.2	263.96	60.15	-28.46
PPT	Pamatai, Tahiti	-17.57	210.42	-16.52	-74.68
PST	Port Stanley, Falkland Is	-51.7	302.11	-38.48	10.59
RAL	Rabbit Lake, Canada	58.22	256.32	67.01	-41.19
RAN	Rankine Inlet, Canada	62.82	267.89	72.47	-24.22
RES	Resolute Bay, Canada	74.69	265.11	83.38	-41.05
SBA	Scott Base, Antarctica	-77.85	166.78	-79.90	-31.99
SCO	Ittoqqortoormiit, Greenland	70.48	338.03	71.50	72.09
SIT	Sitka, Alaska, USA	57.07	224.67	59.76	-80.12
SJG	San Juan, Puerto Rico	18.11	293.85	28.09	10.31
SKT	Maniitsoq, Greenland	65.42	307.1	71.59	37.19
SMI	Fort Smith, Canada	60.02	248.05	67.43	-53.48
SOD	Sodankylä, Finland	67.37	26.63	63.90	107.45
SOR	Sørøya, Norway	70.54	22.22	67.46	105.71
SPA	South Pole Station, Antarctica	-90	–	-73.95	18.61
SPT	San Pablo Toledo, Spain	39.55	355.65	32.08	71.89
STF	Kangerlussuaq, Greenland	67.02	309.28	72.76	40.95
STJ	St Johns, Canada	47.6	307.32	53.87	31.30
SVS	Savissivik, Greenland	76.02	294.9	83.22	34.23
TAL	Taloyoak, Canada	69.54	266.45	78.56	-29.33
THL	Qaanaaq, Greenland	77.47	290.77	85.33	33.59
THY	Tihany, Hungary	46.9	17.54	41.86	91.97
TIK	Tixie, Russia	71.58	129	66.15	-162.08
TRO	Tromsø, Norway	69.66	18.94	66.69	102.68
TRW	Trelew, Argentina	-43.25	294.68	-29.91	4.99
TSU	Tsumeb, Namibia	-19.22	17.7	-30.14	87.12
TUC	Tucson, USA	32.17	249.27	39.77	-45.36
UMQ	Uummannaq, Greenland	70.68	307.87	76.46	42.84
UPN	Upernavik, Greenland	72.78	303.85	79.03	40.68
VAL	Valentia, Ireland	51.93	349.75	49.19	70.39
VIC	Victoria, Canada	48.52	236.58	53.85	-64.08
WNG	Wingst, Germany	53.75	9.07	50.00	86.77
YKC	Yellowknife, Canada	62.48	245.52	69.50	-59.40

Table 1. Locations of the 125 magnetometer sites. Mean CG latitudes and longitudes are averages over all years for which 1-min cadence data was available at that site, computed using the International Geomagnetic Reference Field (IGRF) model. Sites in bold provided 1-s resolution data for this study.

Data Availability Statement

The 1-minute cadence magnetometer data used in this paper is available from https://supermag.jhuapl.edu and described in (Gjerloev, 2012). 1-second cadence UK magnetometer data is available from the British Geological Survey http://www.geomag.bgs.ac.uk/data_service/data/home.html. The MT transfer function data presented in Figure 15 will be available at the UK National Geoscience Data Centre (https://www.bgs.ac.uk/geological-data/national-geoscience-data-centre/) prior to publication.

Acknowledgements

This work was funded by the UK Natural Environment Research Council (NERC) under grants NE/P016715/1 and NE/P017231/1 as part of the UK "Space Weather Impacts on Ground-based Systems" (SWIGS) project. Magnetometer data were provided by SuperMAG (available from https://supermag.jhuapl.edu) and we gratefully acknowledge contributions from the SuperMAG collaborators: Intermagnet; USGS, J. J. Love; CARISMA, PI I. Mann; CANMOS; The S–RAMP Database, PI K. Yumoto and Dr K. Shiokawa; The SPIDR database; AARI, PI Oleg Troshichev; The MACCS program, PI M. Engebretson, Geomagnetism Unit of the Geological Survey of Canada; GIMA; MEASURE, UCLA IGPP and Florida Institute of Technology; SAMBA, PI E. Zesta; 210 Chain, PI K. Yumoto; SAMNET, PI F. Honary; The IMAGE magnetometer network, PI L. Juusola; AUTUMN, PI M. Connors; DTU Space, PI A. Willer; South Pole and McMurdo Magnetometer, PI's L.J. Lanzarotti and A. T. Weatherwax; ICESTAR; RAPIDMAG; British Antarctic Survey; McMac, PI Dr P. Chi; BGS, PI Dr S. Macmillan; Pushkov Institute of Terrestrial Magnetism, Ionosphere and Radio Wave Propagation (IZMIRAN); GFZ, PI Dr J. Matzka; MFGI, PI B. Heilig; IGFPAS, PI J. Reda; University of L'Aquila, PI M. Vellante; BCMT, V. Lesur and A. Chambodut; Data obtained in cooperation with Geoscience Australia, PI M. Costelloe; AALPIP, co-PIs B. Clauer and M. Hartinger; SuperMAG, PI J. W. Gjerloev; Sodankylä Geophysical Observatory, PI T. Raita; Polar Geophysical Institute, A. Yahnin and Y. Sakharov; Geological Survey of Sweden, G. Schwartz; Swedish Institute of Space Physics, M. Yamauchi; UiT the Arctic University of Norway, M. G. Johnsen; Finnish Meteorological Institute, PI K. Kauristie.

References

Adebesin, B. O., Pulkkinen, A., & Ngwira, C. M. (2016). The interplanetary and magnetospheric causes of extreme dB/dt at equatorial locations. *Geophysical Research Letters, 43*(22), 11,501-11,509. https://doi.org/10.1002/2016GL071526

Akasofu, S.-I. (2017). Auroral Substorms: Search for Processes Causing the Expansion Phase in Terms of the Electric Current Approach. *Space Science Reviews, 212*, 341–381. https://doi.org/10.1007/s11214-017-0363-7

Angelopoulos, V., Baumjohann, W., Kennel, C. F., Coroniti, F. V., Kivelson, M. G., Pellat, R., et al. (1992). Bursty bulk flows in the inner central plasma sheet. *Journal of Geophysical Research, 97*, 4027–4039. https://doi.org/10.1029/91JA02701

Apatenkov, S. V., Pilipenko, V. A., Gordeev, E. I., Viljanen, A., Juusola, L., Belakhovsky, V. B., Sakharov, Y. A., & Selivanov, V. N. (2020). Auroral Omega Bands are a Significant Cause of Large Geomagnetically Induced Currents. *Geophysical Research Letters, 47*, e2019GL086677. https://doi.org/10.1029/2019GL086677

Baker, G. J., Donovan, E. F., & Jackel, B. J. (2003). A comprehensive survey of auroral latitude Pc5 pulsation characteristics. *Journal of Geophysical Research: Space Physics, 108*(A10), 1–14. https://doi.org/10.1029/2002JA009801

Barnes, P. R., Rizy, D. T., McConnell, B. W., Tesche, F. M., & Taylor E. R. Jr. (1991). Electric Utility Industry Experience with Geomagnetic Disturbances, ORNL–6665, 1–78, Oak Ridge National Lab., TN, USA. https://doi.org/10.2172/10108452

Beamish, D., Clark, T. D. G., Clarke, E., & Thomson, A. W. P. (2002). Geomagnetically induced currents in the UK: Geomagnetic variations and surface electric fields. *Journal of Atmospheric and Solar-Terrestrial Physics, 64*(16), 1779–1792. https://doi.org/10.1016/S1364-6826(02)00127-X

Bedrosian, P. A., & Love, J. J. (2015). Mapping geoelectric fields during magnetic storms: Synthetic analysis of empirical United States impedances. *Geophysical Research Letters, 42*, 10160–10170. https://doi.org/10.1002/2015GL066636

Beggan, C. D. (2015). Sensitivity of geomagnetically induced currents to varying auroral electrojet and conductivity models. *Earth, Planets and Space, 67*(1). https://doi.org/10.1186/s40623-014-0168-9

Beggan, C. D., Beamish, D., Richards, A., Kelly, G. S., & Alan, A. W. (2013). Prediction of extreme geomagnetically induced currents in the UK high-voltage network. *Space Weather, 11*(7), 407–419. https://doi.org/10.1002/swe.20065

Beggan, C.D., Richardson, G.S., Baillie, O., Hübert, J., Thomson, A.W.P. (2021). Geoelectric field measurement, modelling and validation during geomagnetic storms in the UK. *Journal of Space Weather and Space Climate, 11.* https://doi.org/10.1051/swsc/2021022

Belakhovsky, V., Pilipenko, V., Engebretson, M., Sakharov, Y., & Selivanov, V. (2019). Impulsive disturbances of the geomagnetic field as a cause of induced currents of electric power lines. *Journal of Space Weather and Space Climate*, *9*, A18. https://doi.org/10.1051/swsc/2019015

Boteler, D. H. (2000). Geomagnetic effects on the pipe-to-soil potentials of a continental pipeline. *Advances in Space Research*, *26*(1), 15–20. https://doi.org/10.1016/s0273-1177(99)01020-0

Boteler, D. H. (2021). Modeling Geomagnetic Interference on Railway Signaling Track Circuits. *Space Weather*, *19*(1). https://doi.org/10.1029/2020SW002609

Boteler, D. H., & Pirjola, R. J. (2017). Modeling geomagnetically induced currents. *Space Weather*, *15*(1), 258–276. https://doi.org/10.1002/2016SW001499

Buzulukova, N. (Ed.) (2017). Extreme Events in Geospace : Origins, Predictability, and Consequences. Elsevier. ISBN 9780128127018.

Cagniard, L. (1953). Basic Theory of the magneto-telluric method of geophysical prospecting. *Geophysics*, *18*, 605–635. https://doi.org/10.1190/1.1437915

Campanyà, J., Gallagher, P. T., Blake, S. P., Gibbs, M., Jackson, D., Beggan, C. D. et al. (2019). Modeling geoelectric fields in Ireland and the UK for space weather applications. *Space Weather*, *17*, 216–237. https://doi.org/10.1029/2018SW001999

Cannon, P., Angling, M., Barclay, L., Curry, C., Dyer, C., Edwards, R., et al. (2013). Extreme space weather: impacts on engineered systems and infrastructure. Royal Academy of Engineering. Royal Academy of Engineering, London, U.K. ISBN 1-903496-95-0. http://www.raeng.org.uk/spaceweather

Carrington, R. C. (1859). Description of a Singular Appearance seen in the Sun on September 1, 1859. *Monthly Notices of the Royal Astronomical Society*, *20*, 13–15. https://doi.org/10.1093/mnras/20.1.13

Carter, B. A., Yizengaw, E., Pradipta, R., Halford, A. J., Norman, R., & Zhang, K. (2015). Interplanetary shocks and the resulting geomagnetically induced currents at the equator. *Geophysical Research Letters*, *42*(16), 6554–6559. https://doi.org/10.1002/2015GL065060

Chave, A. D., & Jones, A. G. (2012). The magnetotelluric method. Cambridge University Press. https://doi.org/10.1017/CBO9781139020138

Cliver, E. W., & Dietrich, W. F. (2013). The 1859 space weather event revisited: Limits of extreme activity. *Journal of Space Weather and Space Climate*, *3*, 1–15. https://doi.org/10.1051/swsc/2013053

Coles, S., (2001). An introduction to statistical modeling of extreme values. Springer-Verlag Ltd, London, ISBN 978-1852334598.

Crooker, N. U. (1992). Reverse convection. *Journal of Geophysical Research*, *97*(A12), 19363. https://doi.org/10.1029/92ja01532

Danskin, D. W., & Lotz, S. I. (2015). Analysis of geomagnetic hourly ranges. *Space Weather*, *13*(8), 458–468. https://doi.org/10.1002/2015SW001184

Dimmock, A. P., Rosenqvist, L., Hall, J.-O., Viljanen, A., Yordanova, E., Honkonen, I., et al. (2019). The GIC and geomagnetic response over Fennoscandia to the 7–8 September 2017 geomagnetic storm. *Space Weather*, *17*, 989–1010. https://doi.org/10.1029/2018SW002132

Engebretson, M., Glassmeier, K.-H., Stellmacher, M., Hughes, W. J., & Lühr, H. (1998). The dependence of high-latitude Pc5 wave power on solar wind velocity and on the phase of high-speed solar wind streams. *Journal of Geophysical Research: Space Physics*, *103*(A11), 26271–26283. https://doi.org/10.1029/97ja03143

Engebretson, M. J., Yeoman, T. K., Oksavik, K., Søraas, F., Sigernes, F., Moen, J. I., et al. (2013). Multi-instrument observations from Svalbard of a traveling convection vortex, electromagnetic ion cyclotron wave burst, and proton precipitation associated with a bow shock instability. *Journal of Geophysical Research: Space Physics*, *118*, 2975–2997. https://doi.org/10.1002/jgra.50291

Engebretson, M. J., Pilipenko, V. A., Ahmed, L. Y., Posch, J. L., Steinmetz, E. S., Moldwin, M. B., et al. (2019a). Nighttime magnetic perturbation events observed in Arctic Canada: 1. Survey and statistical analysis. *Journal of Geophysical Research: Space Physics*, *124*, 7442–7458. https://doi.org/10.1029/2019JA026794

Engebretson, M. J., Steinmetz, E. S., Posch, J. L., Pilipenko, V. A., Moldwin, M. B., Connors, M. G., et al. (2019b). Nighttime magnetic perturbation events observed in Arctic Canada: 2. Multiple-instrument observations. *Journal of Geophysical Research: Space Physics*, *124*, 7459–7476. https://doi.org/10.1029/2019JA026797

Engebretson, M. J., Kirkevold, K. R., Steinmetz, E. S., Pilipenko, V. A., Moldwin, M. B., & McCuen, B. A., et al. (2020). Interhemispheric comparisons of large nighttime magnetic perturbation events relevant to GICs. *Journal of Geophysical Research: Space Physics*, *125*, e2020JA028128. https://doi.org/10.1029/2020JA028128

Engebretson, M. J., Pilipenko, V. A., Steinmetz, E. S., Moldwin, M. B., Connors, M. G., Boteler, D. H., et al. (2021). Nighttime magnetic perturbation events observed in Arctic Canada: 3. Occurrence and amplitude as functions of magnetic latitude, local time, and magnetic disturbance indices. *Space Weather*, *19*, e2020SW002526. https://doi.org/10.1029/2020SW002526

Erinmez, I. A., Kappenman, J. G., & Radasky, W. A. (2002). Management of the geomagnetically induced current risks on the national grid company's electric power transmission system. *Journal of Atmospheric and Solar-Terrestrial Physics, 64*(5–6), 743–756. https://doi.org/10.1016/S1364-6826(02)00036-6

Eroshenko, E. A., Belov, A. V., Boteler, D., Gaidash, S. P., Lobkov, S. L., Pirjola, R., & Trichtchenko, L. (2010). Effects of strong geomagnetic storms on Northern railways in Russia. *Advances in Space Research, 46*(9), 1102–1110. https://doi.org/10.1016/j.asr.2010.05.017

Falayi, E. O., Ogunmodimu, O., Bolaji, O. S., Ayanda, J. D., & Ojoniyi, O. S. (2017). Investigation of geomagnetic induced current at high latitude during the storm-time variation. *NRIAG Journal of Astronomy and Geophysics, 6*(1), 131–140. https://doi.org/10.1016/j.nrjag.2017.04.010

Faraday, M. (1832). Experimental researches in electricity. *Philosophical Transactions of the Royal Society, 122*, 125–161. https://doi.org/10.1098/rstl.1832.0006

Fiori, R. A. D., Boteler, D. H., & Gillies, D. M. (2014). Assessment of GIC risk due to geomagnetic sudden commencements and identification of the current systems responsible. *Space Weather, 12*, 76–91. https://doi.org/10.1002/2013SW000967

Freeman, M. P., Forsyth, C., & Rae, I. J. (2019). The Influence of Substorms on Extreme Rates of Change of the Surface Horizontal Magnetic Field in the United Kingdom. *Space Weather, 17*(6), 827–844. https://doi.org/10.1029/2018SW002148

Friis-Christensen, E., McHenry, M. A., Clauer, C. R., & Vennerstrøm, S. (1988). Ionospheric traveling convection vortices observed near the polar cleft: A triggered response to sudden changes in the solar wind. *Geophysical Research Letters, 15*(3), 253–256. https://doi.org/10.1029/GL015i003p00253

Gaunt, C. T. (2016). Why space weather is relevant to electrical power systems. *Space Weather, 14*(1), 2–9. https://doi.org/10.1002/2015SW001306

Gilleland, E. & Katz, R.W. (2016). extRemes 2.0: An extreme value analysis package in R. *Journal of Statistical Software, 72*(8), 1-39. https://doi.org/10.18637/jss.v072.i08

Girgis, R., & Vedante, K. (2012). Effects of GIC on power transformers and power systems. *44th International Conference on Large High Voltage Electric Systems (PES T&D), 7-10 May 2012*, Orlando, FL, USA, 1–8. https://doi.org/10.1109/TDC.2012.6281595

Gjerloev, J. W. (2011) A global ground-based magnetometer initiative, *Eos 90*, 230–231. https://doi.org/10.1029/2009EO270002

Gjerloev, J. W. (2012). The SuperMAG data processing technique. *Journal of Geophysical Research: Space Physics, 117*(9), 1–19. https://doi.org/10.1029/2012JA017683

Hao, Y. X., Zong, Q. G., Zhou, X. Z., Rankin, R., Chen, X. R., Liu, Y., Fu, S. Y., Baker, D. N., Spence, H. E., Blake, J. B., Reeves, G. D., & Claudepierre, S. G. (2019). Global-Scale ULF Waves Associated With SSC Accelerate Magnetospheric Ultrarelativistic Electrons. *Journal of Geophysical Research: Space Physics, 124*, 1525–1538. https://doi.org/10.1029/2018JA026134

Hapgood, M., Angling, M. J., Attrill, G., Bisi, M., Cannon, P. S., Dyer, C., et al. (2021). Development of Space Weather Reasonable Worst Case Scenarios for the UK National Risk Assessment. *Space Weather, 19*, e2020SW002593. https://doi.org/10.1029/2020SW002593

Hartinger, M. D., Shi, X., Lucas, G. M., Murphy, B. S., Kelbert, A., Baker, J. B. H., Rigler, E. J., & Bedrosian, P. A. (2020). Simultaneous Observations of Geoelectric and Geomagnetic Fields Produced by Magnetospheric ULF Waves. *Geophysical Research Letters, 47*, e2020GL089441. https://doi.org/10.1029/2020GL089441

Heyns, M. J., Lotz, S. I., & Gaunt, C. T. (2020). Geomagnetic Pulsations Driving Geomagnetically Induced Currents. *Space Weather, 19*, e2020SW002557. https://doi.org/10.1029/2020sw002557

Hübert, J., Beggan, C. D., Richardson, G. S., Martyn, T., & Thomson, A. W. P. (2020). Differential magnetometer measurements of geomagnetically induced currents in a complex high voltage network. *Space Weather, 18*, e2019SW002421. https://doi.org/10.1029/2019SW002421

Ieda, A., Kauristie, K., Nishimura, Y., Miyashita, Y., Frey, H. U., Juusola, L., et al. (2018). Simultaneous observation of auroral substorm onset in Polar satellite global images and ground-based all-sky images. *Earth, Planets and Space, 70*(1). https://doi.org/10.1186/s40623-018-0843-3

IEEE (2015) IEEE Guide for Establishing Power Transformer Capability while under Geomagnetic Disturbances, IEEE Std C57.163 2015, 3 September 2015, The Institute of Electrical and Electronics Engineers, Inc., ISBN 978-0-7381-9897-2.

Jankee, P., Chisepo, H., Adebayo, V., Oyedokun, D., & Gaunt, C. T. (2020). Transformer models and meters in MATLAB and PSCAD for GIC and leakage dc studies. 2020 International SAUPEC/RobMech/PRASA Conference, SAUPEC/RobMech/PRASA 2020. https://doi.org/10.1109/SAUPEC/RobMech/PRASA48453.2020.9041060

Jorgensen, A. M., Spence, H. E., Hughes, T. J., & McDiarmid, D. (1999). A study of omega bands and Ps6 pulsations on the ground, at low altitude and at geostationary orbit. *Journal of Geophysical Research: Space Physics, 104*(A7), 14705–14715. https://doi.org/10.1029/1998ja900100

Kappenman, J. G. (2003). Storm sudden commencement events and the associated geomagnetically induced current risks to ground-based systems at low-latitude and midlatitude locations. *Space Weather*, *1*(3), 1016. https://doi.org/10.1029/2003sw000009

Kappenman, J. G. (2004), The evolving vulnerability of electric power grids, *Space Weather*, *2*, S01004. https://doi.org/10.1029/2003SW000028.

Kataoka, R., Fukunishi, H., & Lanzerotti, L. J. (2003). Statistical identification of solar wind origins of magnetic impulse events. *Journal of Geophysical Research: Space Physics*, *108*(A12). https://doi.org/10.1029/2003JA010202

Kelbert, A., Egbert, G.D., & Schultz, A. (2011). IRIS DMC Data Services Products: EMTF, The Magnetotelluric Transfer Functions, https://doi.org/10.17611/DP/EMTF.1.

Kelbert, A., Balch, C. C., Pulkkinen, A., Egbert, G. D., Love, J. J., Rigler, E. J., & Fujii, I. (2017). Methodology for time-domain estimation of storm time geoelectric fields using the 3-D magnetotelluric response tensors. *Space Weather*, *15*(7), 874–894. https://doi.org/10.1002/2017SW001594

Kelbert, A., Erofeeva, S., Trabant, C., Karstens, R., & Van Fossen, M. (2018). Taking magnetotelluric data out of the drawer, *Eos*, *99*, https://doi.org/10.1029/2018EO112859

Knipp, D. J. (2011). Understanding space weather and the physics behind it (M. McQuade & D. Kirkpatrick (eds.)). McGraw-Hill Companies, Inc., ISBN 978-0-07-340890-3.

Kozyreva, O. V., Pilipenko, V. A., Belakhovsky, V. B., & Sakharov, Y.A.. (2018). Ground geomagnetic field and GIC response to March 17, 2015, storm. *Earth, Planets and Space*, *70*, 157. https://doi.org/10.1186/s40623-018-0933-2

Lanzerotti, L. J., Konik, R. M., Wolfe, A., Venkatesan, D., & Maclennan, C. G. (1991). Cusp latitude magnetic impulse events: 1. Occurrence statistics. *Journal of Geophysical Research: Space Physics*, *96*(A8), 14009–14022. https://doi.org/10.1029/91ja00567

Laundal, K. M., & Richmond, A. D. (2017). Magnetic coordinate systems. *Space Science Reviews*, *206*, 27. https://doi.org/10.1007/s11214-016-0275-y

Liu, J., Angelopoulos, V., Zhou, X.-Z., and Runov A. (2014). Magnetic flux transport by dipolarizing flux bundles, *Journal of Geophysical Research: Space Physics*,*119*, 909–926. https://doi.org/10.1002/2013JA019395

Love, J. J. and Chulliat, A. (2013), An international network of magnetic observatories, *Eos Transactions, American Geophysical Union*, *94*(42), 373–374. https://doi.org/10.1002/2013EO420001

Love, J. J., Coïsson, P., & Pulkkinen, A. (2016a). Global statistical maps of extreme-event magnetic observatory 1 min first differences in horizontal intensity. *Geophysical Research Letters*, *43*(9), 4126–4135. https://doi.org/10.1002/2016GL068664

Love, J. J., Pulkkinen, A., Bedrosian, P. A., Jonas, S., Kelbert, A., Rigler, E. J., et al. (2016). Geoelectric hazard maps for the continental United States. *Geophysical Research Letters*, *43*(18), 9415–9424. https://doi.org/10.1002/2016GL070469

Love, J. J., Lucas, G. M., Kelbert, A., & Bedrosian, P. A. (2018). Geoelectric hazard maps for the Mid-Atlantic United States: 100 year extreme values and the 1989 magnetic storm. *Geophysical Research Letters*, *45*, 5–14. https://doi.org/10.1002/2017GL076042

McPherron, R. L. (2005). Magnetic pulsations: Their sources and relation to solar wind and geomagnetic activity. *Surveys in Geophysics*, *26*(5), 545–592. https://doi.org/10.1007/s10712-005-1758-7

Milan, S. E., Clausen, L. B. N., Coxon, J. C., Carter, J. A., Walach, M.-T., Laundal, K., Østgaard, N., Tenfjord, P., Reistad, J., Snekvik, K., Korth, H., & Anderson, B. J. (2017). Overview of Solar Wind–Magnetosphere–Ionosphere–Atmosphere Coupling and the Generation of Magnetospheric Currents. *Space Science Reviews*, *206*(1–4), 547–573. https://doi.org/10.1007/s11214-017-0333-0

Milan, S. E., Carter, J. A., Bower, G. E., Imber, S. M., Paxton, L. J., Anderson, B. J., Hairston, M. R., & Hubert, B. (2020). Dual-Lobe Reconnection and Horse-Collar Auroras. *Journal of Geophysical Research: Space Physics*, *125*(10). https://doi.org/10.1029/2020JA028567

Molinski, T. S. (2002). Why utilities respect geomagnetically induced currents. *Journal of Atmospheric and Solar-Terrestrial Physics*, *64*(2002), 1765–1778. https://doi.org/10.1016/S1364-6826(02)00126-8

NERC (2017), Transformer thermal impact assessment: Project 2013-03 (Geomagnetic Disturbance Mitigation), North American Electricity Reliability Corporation, pp. 1–16, Atlanta, GA. Available online: http://www.nerc.com/pa/Stand/Project201303GeomagneticDisturbanceMitigation/Thermal_Impact_Assessment_2017_October_Clean.pdf

Nevanlinna, H., Tenhunen, P., Pirjola, R., Annanpalo, J., & Pulkkinen, A. (2001). Breakdown caused by a geomagnetically induced current in the Finnish telesystem in 1958. *Journal of Atmospheric and Solar-Terrestrial Physics*, *63*(10), 1099–1103. https://doi.org/10.1016/s1364-6826(01)00021-9

Newell, P. T., & Gjerloev, J. W. (2011). Evaluation of SuperMAG auroral electrojet indices as indicators of substorms and auroral power. *Journal of Geophysical Research*, *116*, A12211. https://doi.org/10.1029/2011JA016779

Ngwira, C. M., Pulkkinen, A., Wilder, F. D., & Crowley, G. (2013). Extended study of extreme geoelectric field event scenarios for geomagnetically induced current applications. *Space Weather, 11*, 121–131. https://doi.org/10.1002/swe.20021

Ngwira, C. M., Sibeck, D., Silveira, M. V. D., Georgiou, M., Weygand, J. M., Nishimura, Y., & Hampton, D. (2018). A study of intense local dB/dt variations during two geomagnetic storms. *Space Weather, 16*(6), 676–693. https://doi.org/10.1029/2018SW001911

Nikitina, L., Trichtchenko, L., & Boteler, D. H. (2016). Assessment of extreme values in geomagnetic and geoelectric field variations for Canada. *Space Weather, 14*(7), 481–494. https://doi.org/10.1002/2016SW001386

Oyedokun, D. T. O., & Cilliers, P. J. (2018). Geomagnetically induced currents: A threat to modern power systems. *Classical and Recent Aspects of Power System Optimization* Ed.(s): A. F. Zobaa, S. H. E. Abdel Aleem, & A. Y. Abdelaziz. Academic Press. 421–462. ISBN 9780128124413. https://doi.org/10.1016/B978-0-12-812441-3.00016-1

Pahud, D. M., Rae, I. J., Mann, I. R., Murphy, K. R., & Amalraj, V. (2009). Ground-based Pc5 ULF wave power: Solar wind speed and MLT dependence. *Journal of Atmospheric and Solar-Terrestrial Physics, 71*(2009), 1082–1092. https://doi.org/10.1016/j.jastp.2008.12.004

Pilipenko, V., Kozyreva, O., Belakhovsky, V., Engebretson, M. J., & Samsonov, S. (2010). Generation of magnetic and particle Pc5 pulsations during the recovery phase of strong magnetic storms. *Proceedings of the Royal Society A: Mathematical, Physical and Engineering Sciences, 466*(2123), 3363–3390. https://doi.org/10.1098/rspa.2010.0079

Pilipenko, V. A., Fedorov, E. N., Hartinger, M. D., & Engebretson, M. J. (2019). Electromagnetic fields of magnetospheric ULF disturbances in the ionosphere: Current/voltage dichotomy. *Journal of Geophysical Research: Space Physics, 124*, 109–121. https://doi.org/10.1029/2018JA026030

Pirjola, R. (1984). Estimation of the electric field on the Earth's surface during a geomagnetic variation, *Geophysica, 20*(2), 89–103, ISSN 2324-0741

Pirjola, R. (2010). Derivation of characteristics of the relation between geomagnetic and geoelectric variation fields from the surface impedance for a two-layer earth. *Earth, Planets and Space, 62*(3), 287–295. https://doi.org/10.5047/eps.2009.09.002

Pothier, N. M., Weimer, D. R., & Moore, W. B. (2015). Quantitative maps of geomagnetic perturbation vectors during substorm onset and recovery. *Journal of Geophysical Research: Space Physics, 120*, 1197–1214. https://doi.org/10.1002/2014JA020602

Pulkkinen, A., & Kataoka, R. (2006). S-transform view of geomagnetically induced currents during geomagnetic superstorms. *Geophysical Research Letters, 33*(12), 3–6. https://doi.org/10.1029/2006GL025822

Pulkkinen, A., Viljanen, A., Pajunpää, K., & Pirjola, R. (2001). Recording and occurrence of geomagnetically induced currents in the Finnish natural gas pipeline network. *Journal of Applied Geophysics, 48*(4), 219–231. https://doi.org/10.1016/S0926-9851(01)00108-2

Pulkkinen, A., Viljanen, A., & Pirjola, R. (2006). Estimation of geomagnetically induced current levels from different input data. *Space Weather, 4*(8), S08005. https://doi.org/10.1029/2006SW000229

Pulkkinen, A., Kataoka, R., Watari, S., & Ichiki, M. (2010). Modeling geomagnetically induced currents in Hokkaido, Japan. *Advances in Space Research, 46*(9), 1087–1093. https://doi.org/10.1016/j.asr.2010.05.024

Pulkkinen, A., Bernabeu, E., Eichner, J., Beggan, C., & Thomson, A. W. P. (2012). Generation of 100-year geomagnetically induced current scenarios. *Space Weather, 10*, S04003. https://doi.org/10.1029/2011SW000750

Pulkkinen, A., Bernabeu, E., Thomson, A., Viljanen, A., Pirjola, R., Boteler, D., et al. (2017). Geomagnetically induced currents: Science, engineering, and applications readiness. *Space Weather, 15*, 828–856. https://doi.org/10.1002/2016SW001501

Rogers, N. C., Wild, J. A., Eastoe, E. F., Gjerloev, J. W., & Thomson, A. W. P. (2020). A global climatological model of extreme geomagnetic field fluctuations. *Journal of Space Weather and Space Climate, 10*, 5. https://doi.org/10.1051/swsc/2020008

Russell, C. T., & McPherron, R. L. (1973). Semiannual variation of geomagnetic activity. *Journal of Geophysical Research, 78*(1), 92–108. https://doi.org/10.1029/ja078i001p00092

Saito, T. (1978). Long-period irregular magnetic pulsation, Pi3. *Space Science Reviews, 21*, 427–467. https://doi.org/10.1007/BF00173068

Shepherd, S. G. (2014). Altitude-adjusted corrected geomagnetic coordinates: Definition and functional approximations. *Journal of Geophysical Research: Space Physics, 119*(9), 7501–7521. https://doi.org/10.1002/2014JA020264

Smirnov, M. Y. (2003). Magnetotelluric data processing with a robust statistical procedure having a high breakdown point. *Geophysical Journal International, 152*(1):1–7. https://doi.org/10.1046/j.1365-246X.2003.01733.x

Smith, A. W., Freeman, M. P., Rae, I. J., & Forsyth, C. (2019). The Influence of Sudden Commencements on the Rate of Change of the Surface Horizontal Magnetic Field in the United Kingdom. *Space Weather, 17*(11), 1605–1617. https://doi.org/10.1029/2019SW002281

Thomson, A. W. P., & Flower, S. M. (2021), Modernizing a global magnetic partnership, *Eos, 102*, https://doi.org/10.1029/2021EO156569

Thomson, A. W. P., Gaunt, C. T., Cilliers, P., Wild, J. A., Opperman, B., Mckinnell, L.-A., et al. (2010) Present day challenges in understanding the geomagnetic hazard to national power grids. *Advances in Space Research, 45*(9), 1182–1190. https://doi.org/10.1016/j.asr.2009.11.023

Thomson, A. W. P., Dawson, E. B., & Reay, S. J. (2011). Quantifying extreme behavior in geomagnetic activity. *Space Weather, 9*, S10001. https://doi.org/10.1029/2011SW000696

Tõth, G., Meng, X., Gombosi, T. I., & Rastätter, L. (2014). Predicting the time derivative of local magnetic perturbations. *Journal of Geophysical Research: Space Physics, 119*(1), 310–321. https://doi.org/10.1002/2013JA019456

Trichtchenko, L., & Boteler, D. H. (2004). Modeling geomagnetically induced currents using geomagnetic indices and data. *IEEE Transactions on Plasma Science, 32*(4), 1459–1467. https://doi.org/10.1109/TPS.2004.830993

Vennerstrøm, S. (1999). Dayside magnetic ULF power at high latitudes: A possible long-term proxy for the solar wind velocity? *Journal of Geophysical Research: Space Physics, 104*(A5), 10145–10157. https://doi.org/10.1029/1999ja900015

Viljanen, A. (1997). The relation between geomagnetic variations and their time derivatives and implications for estimation of induction risks. *Geophysical Research Letters, 24*(6), 631–634. https://doi.org/10.1029/97GL00538

Viljanen, A., Nevanlinna, H., Pajunpää, K., & Pulkkinen, A. (2001). Time derivative of the horizontal geomagnetic field as an activity indicator. *Annales Geophysicae, 19*(9), 1107–1118. https://doi.org/10.5194/angeo-19-1107-2001

Viljanen, A., Wintoft, P., & Wik, M. (2015). Regional estimation of geomagnetically induced currents based on the local magnetic or electric field. *Journal of Space Weather and Space Climate, 5*, A24. https://doi.org/10.1051/swsc/2015022

Wang, H., Ridley, A. J., & Lühr, H. (2008). SWMF simulation of field-aligned currents for a varying northward and duskward IMF with nonzero dipole tilt. *Annales Geophysicae, 26*(6), 1461–1477. https://doi.org/10.5194/angeo-26-1461-2008

Watanabe, M., Kabin, K., Sofko, G. J., Rankin, R., Gombosi, T. I., Ridley, A. J., & Clauer, C. R. (2005). Internal reconnection for northward interplanetary magnetic field. *Journal of Geophysical Research: Space Physics, 110*(A6), 1–18. https://doi.org/10.1029/2004JA010832

Watari, S., Kunitake, M., Kitamura, K., Hori, T., Kikuchi, T., Shiokawa, K., et al. (2009). Measurements of geomagnetically induced current in a power grid in Hokkaido, Japan. *Space Weather, 7*(3). https://doi.org/10.1029/2008SW000417

Wei, D., Dunlop, M. W., Yang, J., Dong, X., Yu, Y., & Wang, T. (2021). Intense dB/dt variations driven by near-Earth Bursty Bulk Flows (BBFs): A case study. *Geophysical Research Letters.* https://doi.org/10.1029/2020GL091781

Weigel, R. S., Vassiliadis, D., & Klimas, A. J., (2002) Coupling of the solar wind to temporal fluctuations in ground magnetic fields, *Geophys. Res. Lett., 29*(19), 1915, https://doi.org/10.1029/2002GL014740

Wik, M., Pirjola, R., Lundstedt, H., Viljanen, A., Wintoft, P., & Pulkkinen, A. (2009). Space weather events in July 1982 and October 2003 and the effects of geomagnetically induced currents on Swedish technical systems. *Annales Geophysicae, 27*(4), 1775–1787. https://doi.org/10.5194/angeo-27-1775-2009

Wild, J. A., Yeoman, T. K., Eglitis, P., & Opgenoorth, H. J. (2000). Multi-instrument observations of the electric and magnetic field structure of omega bands. *Annales Geophysicae, 18*(1), 99–110. https://doi.org/10.1007/s00585-000-0099-6

Wild, J. A., Woodfield, E. E., Donovan, E., Fear, R. C., Grocott, A., Lester, M., et al. (2011). Midnight sector observations of auroral omega bands. *J. Geophys. Res, 116*(A5), A00I30. https://doi.org/10.1029/2010JA015874

Winter, L. M., Gannon, J., Pernak, R., Huston, S., Quinn, R., Pope, E., et al. (2017), Spectral scaling technique to determine extreme Carrington-level geomagnetically induced currents effects, *Space Weather, 15*, 713–725, https://doi.org/10.1002/2016SW001586

Wintoft, P. (2005). Study of the solar wind coupling to the time difference horizontal geomagnetic field. *Annales Geophysicae, 23*(5), 1949–1957. https://doi.org/10.5194/angeo-23-1949-2005

Wintoft, P., Wik, M., Lundstedt, H., & Eliasson, L. (2005). Predictions of local ground geomagnetic field fluctuations during the 7-10 November 2004 events studied with solar wind driven models. *Annales Geophysicae, 23*(9), 3095–3101. https://doi.org/10.5194/angeo-23-3095-2005

Wintoft, P, Wik, M, & Viljanen, A. (2015). Solar wind driven empirical forecast models of the time derivative of the ground magnetic field. *Journal of Space Weather and Space Climate*, *5*(A7). https://doi.org/10.1051/swsc/2015008

Wintoft, P, Viljanen, A, & Wik, M. (2016). Extreme value analysis of the time derivative of the horizontal magnetic field and computed electric field. *Annales Geophysicae, 34*, 485–491. https://doi.org/10.5194/angeo-34-485-2016

Zesta, E., Hughes, W. J., & Engebretson, M. J. (2002). A statistical study of traveling convection vortices using the Magnetometer Array for Cusp and Cleft Studies. *Journal of Geophysical Research: Space Physics, 107*(A10), 1–21. https://doi.org/10.1029/1999JA000386

Zhang, X. Y. (2010). ULF waves excited by negative/positive solar wind dynamic pressure impulses at geosynchronous orbit. *Journal of Geophysical Research, 115*, A10221. https://doi.org/10.1029/2009JA015016

Zhao, H., & Zong, Q.-G. (2012). Seasonal and diurnal variation of geomagnetic activity: Russell-McPherron effect during different IMF polarity and/or extreme solar wind conditions. *Journal of Geophysical Research*, *117*, A11222. https://doi.org/10.1029/2012JA017845

Ziesolleck, C. W. S., & McDiarmid, D. R. (1995). Statistical survey of auroral latitude Pc5 spectral and polarization characteristics. *Journal of Geophysical Research*, *100*(A10), 19299. https://doi.org/10.1029/95ja00434